Edinburgh Research Explorer

Investigating the igneous petrogenesis of Martian volcanic rocks using augite quantitative textural analysis of the Yamato nakhlites

Investigating the igneous petrogenesis of Martian volcanic rocks using augite quantitative textural analysis of the Yamato nakhlites

Sammy GRIFFIN [1]*, Arya UDRY [2], Luke DALY [1,3,4], Lucy Victoria FORMAN [5,6], Martin R. LEE [1], and Benjamin E. COHEN [7]

[1]School of Geographical and Earth Sciences, University of Glasgow, Glasgow G12 8QQ, UK
[2]Department of Geoscience, University of Nevada Las Vegas, Las Vegas, Nevada 89154, USA
[3]Australian Centre for Microscopy and Microanalysis, The University of Sydney, New South Wales 2006, Australia
[4]Department of Materials, University of Oxford, Oxford OX1 3PH, UK
[5]Space Science and Technology Centre, School of Earth and Planetary Sciences, Curtin University, GPO Box U1987, Western Australia 6845, Perth, Australia
[6]Department of Earth and Planetary Sciences, Western Australia Museum, Western Australia 6986, Perth, Australia
[7]School of GeoSciences, University of Edinburgh, Edinburgh EH9 3FE, UK
*Corresponding author. E-mail: sammy.griffin@glasgow.ac.uk

Abstract–To better understand volcanism on planetary bodies other than the Earth, the quantification of physical processes is needed. Here, the petrogenesis of the achondrite Martian Yamato (Y) nakhlites (Y 000593, Y 000749, and Y 000802) is reinvestigated via quantitative analysis of augite (high-Ca clinopyroxene) phenocrysts: crystal size distribution (CSD), spatial distribution patterns (SDP), and electron backscatter diffraction (EBSD). Results from CSD and EBSD quantitative data sets show augite to have continuous uninterrupted growth resulting in calculated minimum magma chamber residence times of either 88–117 ± 6 yr or 9–12 yr. All samples exhibit low-intensity S-LS type crystallographic preferred orientation. Directional strain is observed across all samples with intracrystalline misorientation patterns indicative of (100)[001]:(001)[100] (Y 000593 and Y 000802) and $\{110\}<001>$ or $\{110\}^1/_2<110>$ (Y 000749) slip systems. SDP results indicate phenocryst-bearing crystal-clustered rock signatures. Combined findings from this work show that the Yamato nakhlites formed on Mars as individual low-viscosity lava flows or sills. This study shows that through combining these different quantitative techniques over multiple samples, one can more effectively compare and interpret resulting data to gain a more robust, geologically contextualized petrogenetic understanding of the rock suite being studied. The techniques used in this study should be equally applicable to igneous achondrites from other parent bodies.

INTRODUCTION

Igneous processes play an important role in the formation and development of planetary bodies such as the Earth, its Moon, and Mars, with the latter having features that are heavily influenced by volcanic activity (Carr & Head, 2010; Greeley & Spudis, 1981; Grott et al., 2013; Taylor, 2013). Almost all Martian meteorites are igneous rocks (Blamey et al., 2015; McSween & Treiman, 1998; Udry et al., 2020). These samples therefore provide valuable insights into magmatic processes and conditions including planetary differentiation (McSween, 1994; Shearer et al., 2015), volcanic events (Cohen et al., 2017), magmatic evolution (Borg & Drake, 2005; Day et al., 2018; Udry & Day, 2018), and igneous process mechanisms (Longhi, 1991; Rahib et al., 2019; Santos et al., 2015; Udry & Day, 2018).

The Yamato (Y) meteorites (Y 000593, Y 000749, and Y 000802) belong to the nakhlites, which are the second largest group of Martian achondrites (Udry et al., 2020). Found on the same blue ice field in Antarctica (Imae et al., 2003, 2005; Misawa et al., 2003), isotopic

and geochemical data indicate a common parental melt but unidentified source location on Mars (Cohen et al., 2017; Day et al., 2018; Korochantseva et al., 2011; Nyquist et al., 2001; Okazaki et al., 2003; Treiman, 2005). Initial analysis classified the Yamato nakhlites as fall-paired and interpreted the samples as fragments belonging to a single large nakhlite cumulate pile (Imae et al., 2003). However, high-resolution $^{40}Ar/^{39}Ar$ dating of Y 000593 and Y 000749 by Cohen et al. (2017) concluded that they sample at least two different igneous units sourced from a shared parental magma system. The significant increase over the last decade in both number and variability (mineralogical, microstructural, and chemical) of recovered nakhlites supports the conclusion of Cohen et al. (2017) that the group represents multiple igneous bodies rather than the initially hypothesized large cumulate pile (Day et al., 2018; Krämer Ruggio et al., 2020; Tomkinson et al., 2015; Udry & Day, 2018; Udry et al., 2020).

The Yamato nakhlites are excellent samples to use for understanding emplacement through microstructural analysis as they contain some of the lowest measured relative shock levels across all currently identified Martian meteorites (5–14 GPa; Fritz et al., 2005). To summarize their properties, the Yamato nakhlites are unbrecciated mafic igneous rocks of basaltic composition with shape preferred orientation (SPO) indicating clinopyroxene accumulation (Imae et al., 2005). Euhedral augite (high-Ca clinopyroxene 69–77 vol%) is identified as the dominant phase with phenocryst crystal sizes averaging ~1 mm × 0.5 mm. Also present are olivine (11–15 vol%), titanomagnetite (1–4 vol%), and mesostasis (9–16 vol%) comprised of lath-shaped plagioclase with minor augite, pigeonite, olivine, titanomagnetite, K-feldspar, pyrrhotite, apatite, tridymite, and iddingsite (Corrigan et al., 2015; Imae et al., 2003, 2005; Udry & Day, 2018).

A rock's microstructure is defined by the relationships (spatial, orientation, etc.) between and within its constituent components (in this instance crystals). Studies of these relationships provide key insights into physical and material properties, petrogenesis, magmatic evolution, emplacement history (Barsdell, 1988; Corrigan et al., 2015; Daly, Piazolo, et al., 2019; Donohue & Neal, 2018), and post-emplacement deformation (Daly, Lee, et al., 2019; Helmstaedt et al., 1972). Here, two quantitative techniques are used: (1) image processed crystal size distribution (CSD) and related spatial distribution patterns (SDP) and (2) crystallographic analysis using electron backscatter diffraction (EBSD). For ease of comparison between the two presented data sets, the image processed data set (used for CSD and SDP analyses) will henceforth be referred to as CSD and the EBSD data set as EBSD. To aid the reader, a list of acronyms and their definitions used in this paper can be found in Table 1.

The technique of CSD is limited by the resolution of the source images. CSD theory was originally developed to understand crystallization within chemical engineering but has since been applied to understand crystallization processes in igneous rocks (Marsh, 1988). The EBSD technique originates from materials science, where it was developed as a characterization technique (Schwartz et al., 2000). The technique is commonly used via a scanning electron microscope (SEM), which enables the analysis of samples at higher magnifications than traditional optical microscopy (Higgins, 2006; Zhou et al., 2007). This higher magnification is particularly useful when assessing samples of igneous origin, especially fine-grained samples and/or when there is often a limited amount of material available to study (such as meteorites).

Recent CSD and SDP analyses of 11 nakhlites by Udry and Day (2018), including Y 000593 and Y 000749, showed that they consistently exhibit random SPO, that is, they lacked any form of lineation (axis alignment along a singular direction indicating at least two directions of strain), and/or any foliation (axis alignment within a singular plane indicating a single direction of strain; Paterson et al., 1998). The random SPO indicates formation from a larger body with no source of significant external strain. However, recent EBSD investigations of four nakhlites by Daly, Lee, et al. (2019) identified consistent weak–moderate foliation, with some of the meteorites also exhibiting lineation crystallographic preferred orientation (CPO) and SPO. The results from Daly, Piazolo, et al. (2019) imply diverse formational histories for the nakhlites, where the lineation results indicate an origin that is not solely driven by crystal settling (Holness, 2007; Holness et al., 2007; Hunter, 1996). In this paper, CSD and EBSD analyses have been applied to further physically constrain the petrogenesis of the individual Yamato nakhlite stones, and so to better understand their igneous emplacement prior to their impact ejection from Mars.

MATERIALS AND METHODS

Augite was analyzed in five polished thick sections representing all three Yamato nakhlites: Y 000593 (106-A and 127-A), Y 000749 (64-A and 72-A), and Y 000802 (36-A). Augite phenocrysts were chosen for two reasons: (1) their high (~60–80 vol%) modal abundance in the nakhlites (Imae et al., 2003; Treiman, 2005; Udry & Day, 2018) and (2) their crystal shape enables the short crystallographic <001>, that is, <c> axis (i.e., CPO) to be used as a proxy for the long shape axis (SPO) to assess preferred orientation (Daly, Piazolo, et al., 2019; Morimoto et al., 1988). Our analysis includes previous CSD and SDP results from Udry and Day (2018) for sections Y 000593 (106-A) and Y 000749 (72-A) that are

Table 1. Acronyms used in this paper and their definitions.

Acronym	Definition
A aka "A-type"	Component of the BA-Index referring to girdle CPO in the crystallographic [100] aka [a] axis
B aka "B-type"	Component of the BA-Index referring to lineation CPO in the crystallographic [010] aka [b] axis
BA-Index	The A and B crystallographic axes index; shows the relationship between the perpendicular <a> and <b> crystallographic axes where 1 = complete P_{010} CPO (B-type) and 0 = complete G_{100} CPO (A-type)
CPO	Crystallographic preferred orientation
CSD	Crystal size distribution
EBSD	Electron backscatter diffraction
EDS	Energy-dispersive X-ray spectroscopy
GOS	Grain orientation spread; measurement of the angle deviation within crystals across a given data set
IPF	Inverse pole figure
J-Index	A type of CPO index which uses the second moment of an ODF, where the ODF is the distribution of discrete crystal orientation data in Euler angle space
L aka "L-type"	Component of the LS-Index, referring to lineation or point CPO within the crystallographic [010] aka [b] axis
LS-Index	The B and C crystallographic axes index; shows the relationship between the perpendicular <b> and <c> crystallographic axes where 1 = indicates complete P_{010} CPO (L-type) and 0 = complete G_{001} CPO (S-type)
MAD	Mean angular deviation; an assessment of Kikuchi pattern quality
M-Index	Misorientation index (a type of CPO index)
MOS	Maximum orientation spread; maximum angle deviation angle from the mean crystal orientation
MUD	Multiples of uniform density, an expression of ODF
ODF	Orientation distribution function
OPPG	One point per grain
PGR	Point (a.k.a. lineation), girdle (a.k.a. foliation), random ternary endmembers of Eigenvalue analysis (a type of CPO index)
S or "S-type"	Component of the LS-Index, referring to "schistose" or girdle CPO within the crystallographic [001] aka [c] axis
SDP	Spatial distribution pattern
SEM	Scanning electron microscope
SPO	Shape preferred orientation

supplemented by new EBSD analysis described here. All samples analyzed in this study were provided by the Japanese National Institute of Polar Research (NIPR) as premade thick sections and as such were not cut with respect to any SPO nor an external common reference point. Meteorite samples typically lack external reference points. For this study, an arbitrary principal orientation was defined based on the EBSD maps (Fig. 1) to enable consistency in comparing and presenting data between the different sections where: Y = top–bottom direction of the thick section, X = left–right direction of the thick section, and Z = direction perpendicular to the plane of the thick section. Additionally, for ease of comparison between CSD and EBSD data sets, all EBSD measurements are reported in mm or mm^2 rather than the more typical units of μm and $μm^2$.

Electron Microscopy

In preparation for EBSD analysis, each of the five thick sections underwent a fine mechanical polish using 1 μm then 0.3 μm aluminum spheres suspended in glycol for 5 min before being chemically polished for 4 h using 0.1 μm colloidal silica suspended in an NaOH solution. These polishing steps were followed by the application of an ~10 nm thick conductive carbon coat using a sputter coater.

All samples were studied by SEM. Backscatter and forescatter electron images, and energy-dispersive X-ray spectroscopy (EDS) and EBSD data were obtained at the ISAAC imaging center, University of Glasgow. The SEM used was a Zeiss Sigma Field Emission Gun Variable Pressure Scanning Electron Microscope (FEG-VP-SEM) operating Oxford Instruments AZtec analysis software v3.3. Conditions were tilt 70°, high vacuum (3.5×10^{-4} Pa) accelerating voltage 20 keV, aperture 120 μm, beam current 4.1 nA (full analysis settings for each studied section are available in Appendix S1). EDS analyses were collected simultaneously with the EBSD data using an Oxford Instruments X-Max 80 mm^2 silicon drift detector energy-dispersive X-ray spectrometer and NordlysMax^2 EBSD detector.

Step sizes for each individual EBSD measurement (ranging 3–5 μm) were chosen to maximize the surface area covered by the maps and ensure data collection over reasonable time frames (<2 days), while still being smaller than each section's augite crystals. For data processing, the phase augite (crystallographic axes $a = 10.97 < b = 10 < c = 5.96$ Å) was selected. Kikuchi diffraction patterns were assessed to provide reasonable mean angular deviation (MAD) values (0.51–0.72) that were in range of acceptable indexing values for geological specimens (Prior et al., 2009). EBSD data were noise-reduced using Oxford Instruments HKL
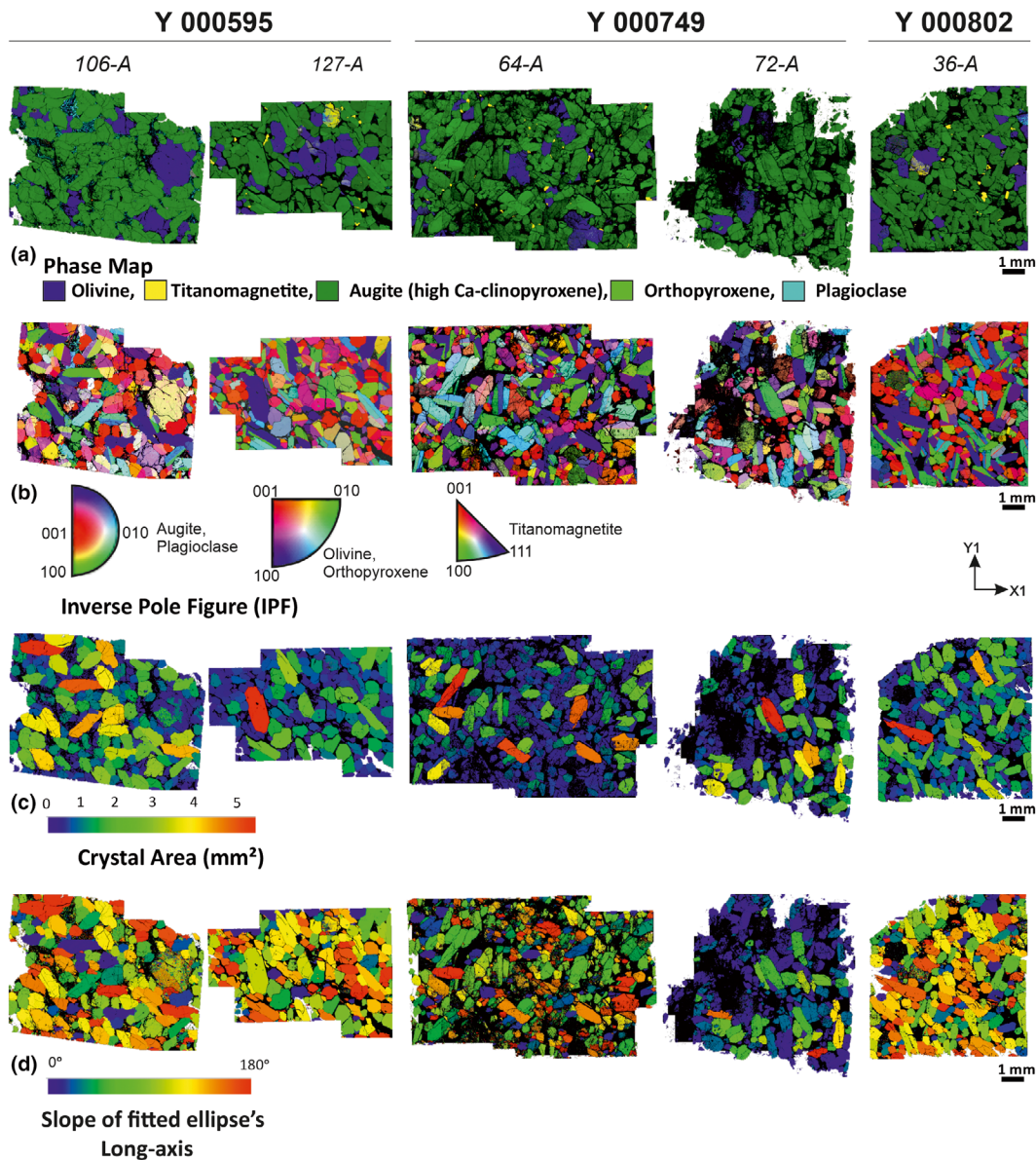
Fig. 1. EBSD results from the Yamato nakhlites. a) Phase map showing augite (px, green) as the dominant phase within all samples. Other phases indicated are olivine (blue), orthopyroxene (lime green), plagioclase (aqua), and magnetite (yellow). Px abundance in vol% is as follows: 54% Y 000593 (106-A), 53% Y 000593 (127-A), 45% Y 000749 (64-A), 32% Y 000749 (72-A), 61% Y 000802 (36-A). For the full breakdown of modal mineralogy, please refer to supporting information. b) Inverse pole figure (IPF) maps oriented in the Z direction (axes perpendicular relative to the map plane). c) Crystal area referring to the thick section 2-D SPO. d) Slope angle relating calculated fitted ellipse long axis relative to the map plane. Fitted ellipse major axis represents the true SPO crystal long axis corrected for crystallographic orientation using the <c>crystallographic axis (coupled to augite's long shape axis).

Channel 5 software as per standard procedure; a single wildspike correction followed by an iterative 8, 7, and then 6 points nearest neighbor zero solution reduction to remove erroneous data points (mis-indexed and non-indexed points) and facilitate crystal definition without generating significant artifacts within the data set (Bestmann & Prior, 2003; Daly, Lee, et al., 2019; Forman et al., 2016, 2019; Watt et al., 2006). EDS scans encompassing the entire thick section were acquired for Y 000593 (127-A), Y 000749 (64-A), and Y 000802 (36-A) to incorporate regions outside the EBSD maps to assist CSD and SDP analyses. These larger

scans were acquired on the Zeiss SEM at a 0° tilt angle, under high vacuum (3.5×10^{-4} Pa), with a field of view of 0.6×0.8 mm per frame, working distance 8.5 mm, 20 keV, and a 4.1 nA beam current.

SPO and CPO Analyses

Electron Backscatter Diffraction

Individual augite crystals were identified via HKL Channel 5's automated "grain detect" algorithm. Crystal boundaries were determined based on a >10° internal crystallographic misorientation threshold of each neighboring pixel, accounting for visually identified twin boundaries (180° rotation around augite's [100], [001], [204], or [104] planes). Crystals <10 pixels in size were removed from the complete data set as they would constitute too few data points to robustly sample the mineral and define its crystal size based on the scan resolution, the step size, and the crystal fracturing within each section (Forman et al., 2019; Watt et al., 2006). To enable consistent comparison between EBSD and CSD data sets, crystals <0.3 mm (the resolution limit of the CSD data set) were ignored for CPO and SPO analyses. Prior to intercrystalline CPO and SPO analyses, a one point per grain (OPPG) data reduction was applied to each sample, where the OPPG subset was visually checked for artifacts against Euler and inverse pole figure (IPF) results and an additional manual reduction applied. This manual reduction removed any excess crystallites associated with fractured crystals, whose boundaries exceeded the >10° internal misorientation threshold.

EBSD SPO was derived using the slope angle calculated from the best-fit ellipse algorithm in Oxford Instruments' HKL Channel 5 Tango module. This algorithm was used to calculate crystal area, length of the long shape axis, and slope of the ellipse relative to the thick section surface.

EBSD intercrystalline CPO was determined using the reduced OPPG subsets (n_{OPPG}, Table 4) and plotted on lower hemisphere equal area projections (pole figures) using HKL Channel 5's Mambo software module. Pole figures were plotted using the following settings: cluster 3°, half width 15°, with the maximum uniform density (MUD; i.e., relative density of data points) value ranging 0–5 (exceeds individual scan MUD values) to enable comparison between samples.

The strength and intensity of CPO in each sample were quantified using three combined CPO calculations: M-index, J-index, and Eigenvalue analysis (Bunge, 1982; Skemer et al., 2005; Vollmer, 1990), via the MATLAB toolbox "MTEX" (Bachmann et al., 2011). Data used for these calculations were sourced from the raw exported EBSD data. CTF files underwent noise reduction (equivalent to Channel 5's Wildspike), crystal boundaries established at 10° misorientation between pixels, and all crystals <0.3 mm were removed (n_{MTEX}, Table 4). CPO was assessed using the code of Daly, Piazolo, et al. (2019) with amendments according to Mainprice et al. (2015). Here, the CPO strength values and parameters are defined based on available pyroxene data sourced from compositionally similar terrestrial igneous rocks (i.e., plutonic intrusive or extrusive basaltic igneous specimens).

M-index CPO results will sit between 0 (random CPO) and 1 (single crystal CPO; Skemer et al., 2005). The calculation attributes equal weighting to all crystallographic axes and assesses the amount of rotation required for two neighboring crystals to be aligned (Skemer et al., 2005). Stable M-Index values require <2% convergence, where the exact number of crystals is dependent on the CPO intensity of the specimen. For the nakhlites, ~300 crystals are required.

J-index utilizes the crystal's Euler angles, where CPO results theoretically increase from 0 (random CPO) to infinity (single crystal CPO; Bunge, 1982). For this study, CPO strengths are classified using the same ranges as Daly, Piazolo, et al. (2019), that is, where low CPO =1.40–1.80, low–medium CPO = 1.80–2.40, medium CPO = 2.40–5.00, medium–strong CPO = 5.00–12.00, and strong CPO = >12. Statistically relevant data sets for J-Index results are also directly linked to the intensity of the CPO, where the number of crystals required (~300) increases with decreasing intensity (Ismaïl & Mainprice, 1998).

Eigenvalue measurements assess the shape, intensity, and strength of CPO. These results are typically reported for each crystallographic axis as a normalized fraction between three CPO endmembers: random (R), point maxima (lineation; P), and girdle (foliation; G), where the combined PGR value for each axis is equal to 1 (Vollmer, 1990). Due to the nature of geological materials, pure 100% endmembers are uncommon, and therefore, strong CPO is considered to have representative Eigenvalues of ~50% (Boneh & Skemer, 2014; Daly, Piazolo, et al., 2019). Eigenvalue analysis here uses the same parameters reported in Daly, Piazolo, et al. (2019), which infers random CPO as R >90%, weak CPO (P and G 10%–30%), moderate CPO (P and G 30%–50%), and strong fabric (P and G >50%). Additional CPO shape information can be calculated from relating augites' two sets of perpendicular crystallographic axes: [010] and [001] using the LS-Index, and [100] and [010] using the BA-Index. LS and BA indices were calculated using the following equations:
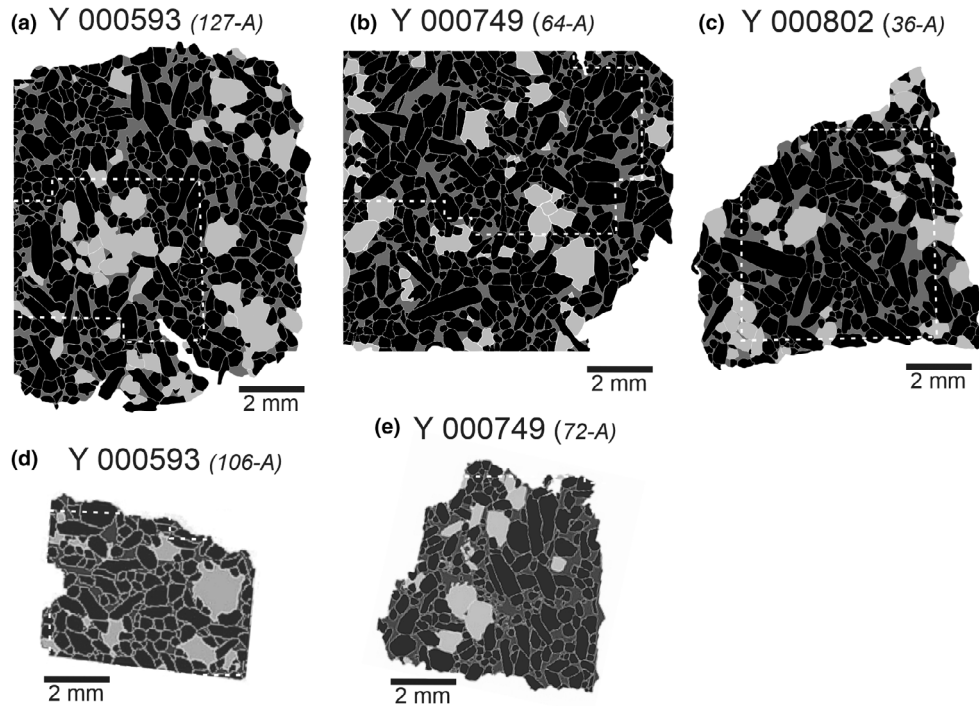
Fig. 2. Manually outlined crystals identified for CSD analysis (CSD data set) where augite (high-Ca pyroxene; px) is black, olivine (ol) is light gray, mesostasis phases (mes) are dark gray. Abundance of phases is in vol%: a) Y 000593 (127-A; px: 67%, ol: 16%, mes:17%); (b) Y 000749 (64-A; px: 70%, ol: 11%, mes: 19%); (c) Y 000802 (36-A; px: 66%, ol: 16%, mes: 18%); (d) Y 000593 (106-A; px:72.1%, ol: 14.9%, mes: 12.9%); and (e) Y 000749 (72-A; px: 68.8%, ol: 10.8%, mes: 20.3%). All images are at the same scale. Images (d) and (e) and associated CSD results are originally published in Udry and Day (2018). For the full mineralogical breakdown, please refer to supporting information. White dashed lines indicate EBSD analysis regions shown in Fig. 1.

$$LS = \frac{1}{2}\left[2 - \left(\frac{P_{010}}{G_{010} + P_{010}}\right) - \left(\frac{G_{001}}{G_{001} + P_{001}}\right)\right] \quad (1)$$

$$BA = \frac{1}{2}\left[2 - \left(\frac{P_{010}}{G_{010} + P_{010}}\right) - \left(\frac{G_{100}}{G_{100} + P_{100}}\right)\right] \quad (2)$$

where P_x and G_x refer to the Eigenvalue P and G results of a given crystallographic axis (x). Calculated index values = 1 (L- or B-type) indicate lineation-dominant CPO and values = 0 (S- or A-type) indicate foliation type CPO for the respective index.

The level of internal crystal deformation for each sample was investigated using average grain orientation spread (GOS), the mean deviation angle from the crystal's average orientation, and the maximum orientation spread (MOS), the highest angle difference across the sample, using HKL Channel 5's grain detect algorithm. Intracrystalline misorientation patterns, which allude to the activated slip systems within a crystal's internal grain boundaries, were processed from the EBSD data set prior to OPPG reduction. Crystal and sample reference plots were created using HKL Channel 5's Mambo software module using the

following settings: cluster 3°, half width 15°, with the MUD values ranging 0–5 to enable comparability between different EBSD scans.

CSD and SDP from IP-QTA Analysis

New augite population CSD and SDP analyses for sections Y 000593 (127-A), Y 000749 (64-A), and Y 000802 (36-A) were conducted following the same collection and data processing procedure as Udry and Day (2018), including the same user (Udry). All final images (Fig. 2), which form the foundation of the resultant CSD data set, were hand drawn using Adobe© Illustrator© and were processed and corrected using ImageJ, CSDslice, and CSDcorrections software packages (Higgins, 2006; Morgan & Jerram, 2006; Schneider et al., 2012). Construction of Fig. 2 images was aided by visual identification of crystal boundaries using several tools: (1) X-ray elemental maps from the University of Nevada Las Vegas (UNLV) JEOL JXA-8900 electron microprobe (operated at 15 kV acceleration voltage, 60 nA beam current, pixel dwell time of 9 s, step size 2 μm); (2) reflected light microscopy using a Nikon LV100POL microscope at UNLV; (3) EBSD IPF, phase, and Euler maps and EDS (combination of Al, Fe, Mg,

Table 2. Yamato nakhlite SDP analysis (CSD data set).

	Y 000593		Y 000749		Y 000802
	106-A*	127-A	64-A	72-A*	36-A
R	1.43	1.44	1.39	1.36	1.41
% melt	31.2	33.4	29.7	37.3	33.4
% crystallinity (all phases)	68.8	66.6	70.3	62.7	66.7

Both % melt and crystals have been corrected for SDP analysis from the CSD data set. R = the ordering of crystals based on distance and quantity of neighboring crystals from a given grains center (R <1.65 clustered and R >1.65 ordered).
*Data from Udry and Day (2018).

P, and S) elemental maps collected using the FEG-VP-SEM at the University of Glasgow.

Modal abundances of different crystalline phases and melt percent using pixel counting from the X-ray elemental maps were calculated from the CSD data set (Table 2; for a full breakdown, the reader is referred to supporting information).

Crystallization kinetic and mechanical processes (cooling rate, crystal growth rate, fractionation, accumulation, and crystal coarsening) were assessed using the following steady-state crystal population equation applied to the CSD data set:

$$n = n^{0^{(L/G\tau)}} \qquad (3)$$

where n is the crystal population density, n^0 is the final crystal nucleation density (i.e., the slope intercept derived from plotting the negative natural log of measured crystal population density versus crystal size; Fig. 3), L is the crystal size, G is the calculated growth rate, and τ is the residence time (Cashman & Marsh, 1988; Marsh, 1988, 1998).

SDP analysis uses CSD data to assess crystal population ordering, crystal frameworks, and rock formation processes (e.g., compaction, crystal orientation, and flow settling). SDP plots percentage melt against R, the ratio of predicted versus observed crystal center distance for a 2D data set, defined as:

$$R = \sqrt[2]{\rho \Sigma r / N} \qquad (4)$$

where ρ is the observed crystal population density, r is the distance between the center of a crystal and the center of its nearest neighboring crystal taken from the corrected intercept of the short:intermediate:long axes, and N is the total number of crystals measured (Jerram, 2003; Jerram et al., 1996). Note for these analyses, melt percentage refers to anything that is not augite (i.e., includes olivine, finer grained mesostasis
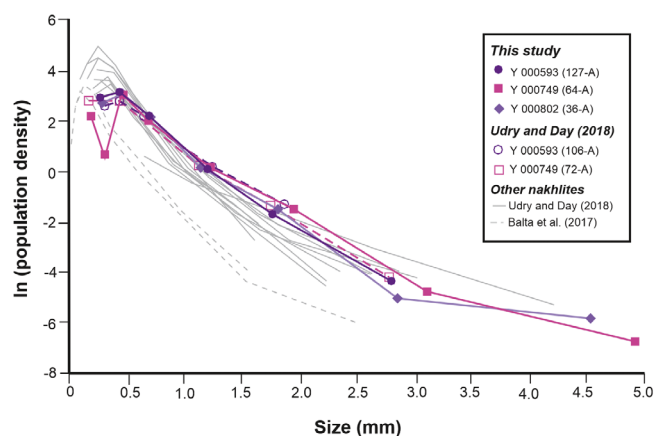

Fig. 3. Crystal size distribution (CSD) profiles for augite based on the CSD data set (Table 3). The three Yamato thick sections: Y 000593 (127-A solid dark purple circle and 106-A open dark purple circle), Y 000749 (64-A solid pink square and 72-A open pink square), and Y 000802 (36-A solid light purple diamond). CSD profiles for sections Y 000593 (106-A) and Y 000749 (72-A) having been previously reported alongside other nakhlites (solid gray lines) by Udry and Day (2018) and Balta et al. (2017; gray-dashed lines). CSD results from the present study are consistent with the distribution reported by Udry and Day (2018).

material [crystals <0.3 mm], and void space within the sample).

RESULTS

Augite abundances were determined using data sets from both CSD (Table 3) and EBSD (post-OPPG data reduction; Table 4). Higher numbers of crystals per polished section were detected within the EBSD data set than the CSD data set despite EBSD analyzing smaller areas of each sample (Figs. 1 and 2). This higher number of detected crystals is in part due to the fractured nature of the analyzed augite crystals. Thus, the reduced OPPG EBSD data set is referred to when reporting results, as it accounts for crystal fracturing within the samples.

Augite Morphology

Augite crystals within all three Yamato nakhlites are euhedral with zoned edges. Measured averaged crystal sizes reported below indicate the samples to be fine-grained according to igneous terminology (Winter, 2013) rather than coarse-grained as previously reported (Treiman, 2005).

Augite CSD results using the long shape axis produce an average length of 0.45 mm for Y 000593 (127-A), 0.51 mm for Y 000749 (64-A), and 0.46 mm for Y 000802 (36-A). These measurements all lie within

Table 3. Augite grain statistics from CSD (grains ≥0.3 mm shape diameter, unless stated).

	Y 000593		Y 000749		Y 000802
	106-A[a]	127-A	64-A	72-A[a]	36-A
Area (mm^2)	22	69	86	34	10
n	118	419	446	193	227
R^2	0.84	0.9	0.87	0.84	0.88
Shape aspect ratio[b]	1.00:1.25:1.90	1.00:1.15:1.60	1.00:1.30:2.00	1.00:1.30:1.80	1.00:1.20:1.70
R	1.44	1.43	1.39	1.35	1.41
Augite length (mm)					
Av. length	0.47	0.45	0.51	0.45	0.46
SD (1σ)	0.27	0.27	0.29	0.33	0.31
Max length	1.46	1.78	2.66	2.34	2.87
Min length	0.09	0.04	0.11	0.08	0.12
Slope (mm^{-1})					
All grains	−2.85	−3.45	−2.9	−3.03	−3.43
SD	0.25	0.14	0.12	0.19	0.21
Grains ≥0.3 mm	−2.72	−3.61	−3.03	−2.84	−3.43
Slope intercept					
All grains	3.89	4.43	4.04	3.86	4.39
SD	0.23	0.20	0.11	0.16	0.17
Grains ≥0.3 mm	3.77	4.61	4.18	3.70	4.39
Px (%)	72.1	67.2	70.4	68.8	66.8
Alignment factor	0.10	0.17	0.12	0.12	0.17
Residence T (yr)					
T[c] (all grains)	111	92	109	105	92
T[c] (grains ≥0.3 mm)	117	88 ± 4	105 ± 4	112	88 ± 6
T[d] (grains ≥0.3 mm)	12	9	10	11	9

N = number of grains; R^2 = coefficient of determination; R = R value (ratio between predicted and measured grain center); SD = standard deviation; T = residence time.
[a]Data from Udry and Day (2018).
[b]Average augite shape aspect ratio (short:intermediate:long).
[c]Based clinopyroxene growth rates of 10–10 mm s^{-1} from Leu (2010).
[d]Based on silicate growth rates of 10–9 mm s^{-1} from Cashman and Marsh (1988) and Jerram (2003).

1σ of each other (Table 3) and are within error of the measurements from Udry and Day (2018) (0.47 and 0.45 mm, for Y 000593 [106-A] and Y 000749 [72-A], respectively). The best fit ratio corresponding to the short:intermediate:long shape axis ratio of the pyroxene population ranges from 1.00:1.15:1.60 for Y 000593 (127-A), to 1.00:1.20:1.70 for Y 000802 (36-A), to 1.00:1.30:2.00 for Y 000749 (64-A; Table 3). These axis length ratios (Table 3) sit within range of previous reported CSD results of 1.00:1.25:1.90 for Y 000593 (106-A) and 1.00:1.30:1.80 for Y 000749 (72-A; Udry & Day, 2018). All five augite CSD profiles exhibit a negative linear correlation (Fig. 3), with a downturn (i.e., a slight positive slope) for crystal sizes ≤0.3 mm. An anomalous decrease in the abundance of measured 0.4 mm sized crystals is observed in Y 000749 (64-A). Excluding crystal sizes below 0.3 mm, the slopes vary from −3.03 mm^{-1} in Y 000749 (64-A) to −3.43 mm^{-1} in Y 000802 (36-A) and −3.61 mm^{-1} in Y 000593 (127-A; Table 3; Figs. 3 and 4). Similar results were reported by Udry and Day (2018): −2.72 mm^{-1} in Y 000593

(106-A) and −2.84 mm^{-1} in Y 000749 (72-A) (Balta et al., 2017).

EBSD data identify 1.8%–11.6% elongate crystals oriented in the map plane (Table 4). A subset was created to assess crystal shape more accurately (Table 4: elongate grains oriented in map plane), using crystals with the <001> crystallographic axis oriented parallel to the map plane (±5°), highlighting the importance of slope angle corrections when assessing crystal habit and SPO data. GOS values across the samples show low levels of intragrain deformation ranging 0.48–1.24° (Table 4). HKL Channel 5 best-fit ellipse algorithm calculates aspect ratios that cluster around 1–3 with higher ratios trending toward larger crystals (Fig. 5). Calculated crystal areas show Y 000593 (106-A) and Y 000749 (64-A) to have the largest range (0.1–0.5 mm^2; Fig. 6), and Section Y 000593 (127-A) to have the smallest range (0.1–0.3 mm^2; Fig. 6). Phenocryst long shape axis values derived from the crystallographic <c> axis range between 0.3 and 0.6 mm (Fig. 6), averaging 0.35–0.44 mm in length (Table 4).

Table 4. Augite grain statistics from EBSD (grains ≥0.3 mm shape diameter).

	Y 000593		Y 000749		Y 000802
	106-A	127-A	64-A	72-A	36-A
Augite indexed (%)	53.7	52.6	44.7	31.9	61.3
$n_{(all\ data)}$	1035	395	7450	2478	670
n_{OPPG}	93	109	197	111	138
Shape long axis length (mm)					
Av.	0.44	0.35	0.44	0.42	0.43
SD	0.13	0.14	0.12	0.88	0.14
MOS (°)	4.36–6.26	2.64–6.78	4.44–8.54	1.42–6.26	2.84–35.95
Av.	5.42	4.61	6.15	3.64	13.36
SD	0.84	2	1.13	1.52	11.61
GOS (°)	0.42–3.17	0.37–1.07	0.52–2.13	0.19–0.98	0.45–3.12
Av.	1.13	0.58	0.90	0.48	1.24
SD	1.36	0.33	0.53	0.25	1.16
Aspect ratio					
A-axis					
Av.	–	–	1.63	3.51	1.65
n_A	0	0	4	2	5
SD	–	–	0.45	0.08	0.68
B-axis					
Av.	–	–	1.40	–	–
n_B	0	0	1	0	0
SD	–	–	–	–	–
C-axis					
Av.	1.86	1.24	2.11	2.36	2.11
n_C	4	2	6	7	11
SD	0.79	0.20	0.95	0.72	2.21
All axes					
Av.	1.86	1.24	1.91	2.62	2.02
n_T	4	2	10	9	16
SD	0.79	0.20	0.80	0.81	1.91
Elongate crystals oriented in map plane (%)	4.3	1.8	5.1	8.1	11.6
CPO grains					
n_{MTEX}	287	299	508	303	383
M-Index	0.03	0.03	0.04	0.04	0.02
J-Index	3.55 ± 0.71	4.76 ± 0.23	2.92 ± 0.14	3.79 ± 0.18	2.72 ± 0.14
Eigenvalue					
Point (P)					
[100]	0.04	0.06	0.14	0.13	0.12
[010]	0.13	52.14	0.07	0.08	0.08
[001]	0.17	0.10	0.10	0.18	0.15
Girdle (G)					
[100]	0.19	0.11	0.04	0.02	0.15
[010]	0.09	0.08	0.16	0.24	0.05
[001]	0.27	0.41	0.44	0.38	0.19
Random (R)					
[100]	0.78	0.78	0.89	0.84	0.73
[010]	0.78	0.79	0.71	0.68	0.87
[001]	0.56	0.49	0.45	0.44	0.65

Table 4. *Continued.* Augite grain statistics from EBSD (grains ≥0.3 mm shape diameter).

	Y 000593		Y 000749		Y 000802
	106-A	127-A	64-A	72-A	36-A
LS index	0.40	0.28	0.37	0.54	0.41
BA index	0.29	0.36	0.58	0.81	0.41
$MUD_{max-min}$	0.23–5.92	0.26–2.91	0.46–2.22	0.22–4.78	0.59–2.26

n_A = number of grains in subset A with <a> axis parallel (±5°) to the plane of the sample; n_B = number of grains in subset B with <b> axis (±5°) to the plane of the sample; n_C = number of grains in subset C with <c> axis (±5°) to the plane of the sample; n_T = total number of grains with any axis parallel (±5°) to the plane of the sample; LS index = assessment of lineation (L = 1) and foliation (S = 0) fabrics between {010} and {001} eigenvalue results from Equation 1; BA index = assessment crystallographic preference between {010} (B = 1) and {100} (A = 0) from Equation 2.

n = number of grains; OPPG = one point per grain; Av. = average; SD = standard deviation; CPO = crystal preferred orientation; MUD = multiples of uniform density.
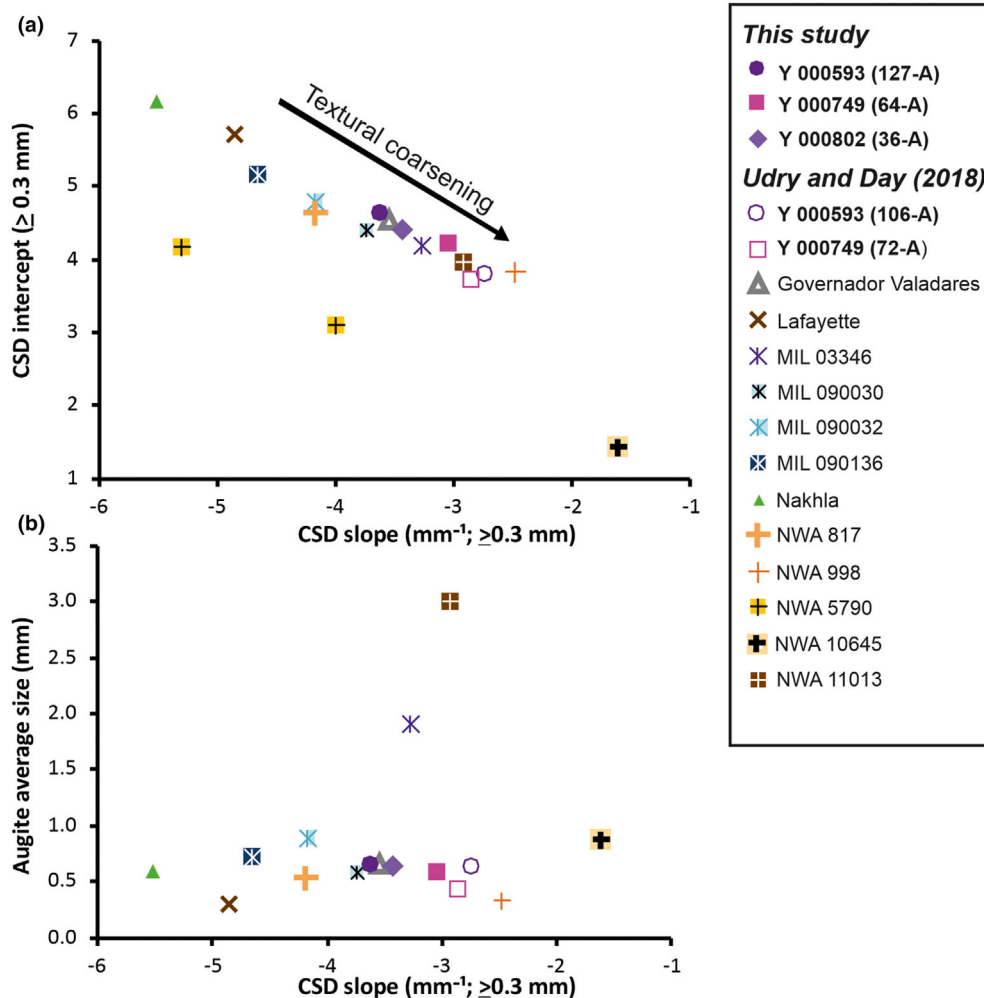

Fig. 4. CSD data of Yamato augite (CSD data set of crystals ≥0.3 mm). a) CSD slope (mm^{-1}) versus intercept (summarized Table 3). b) CSD slope versus augite average size (mm; summarized in Table 3). Samples from the present study exhibit a lower slope in comparison with previously analyzed thick sections of the same meteorites but lie within the overall nakhlite trend (Udry & Day, 2018).
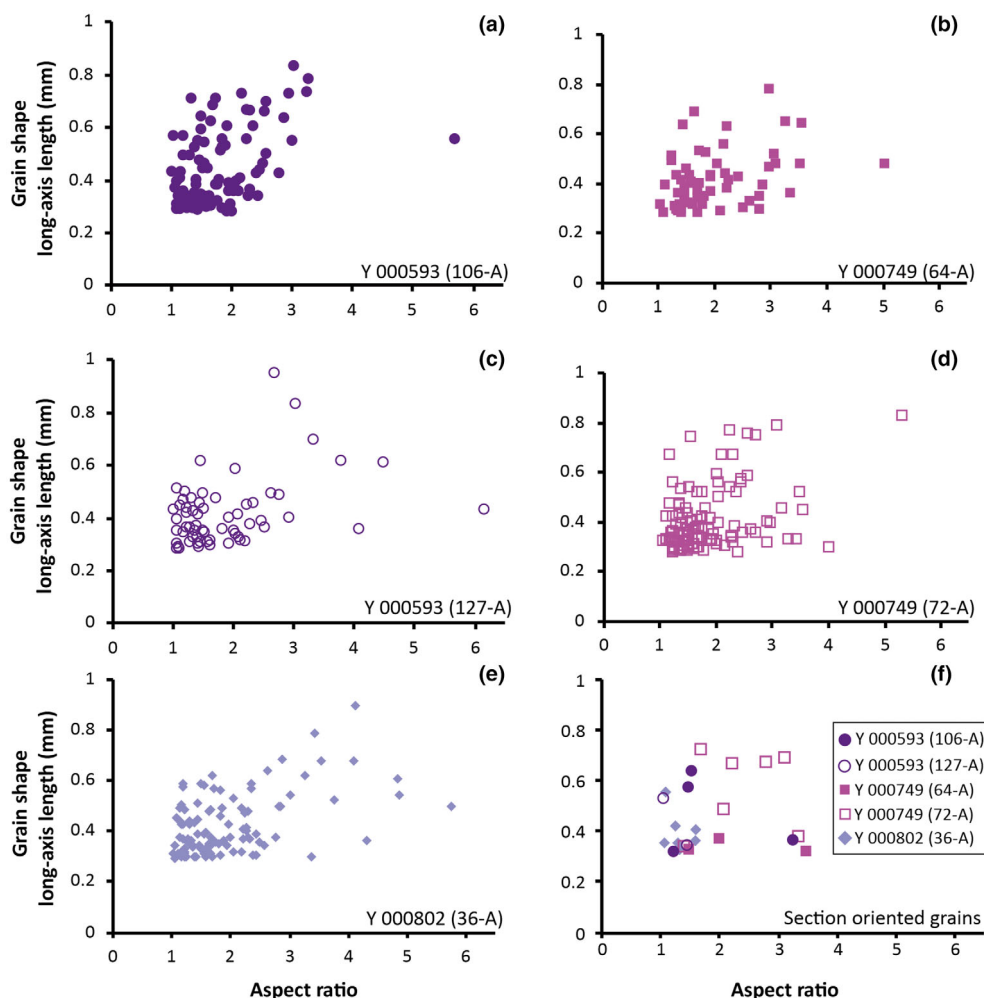
Fig. 5. Crystal shape long axis length versus aspect ratio of Yamato nakhlites for grains ≥0.3 mm from EBSD data set (summarized in Table 4). a) Y 000593, 106-A; (b) Y 000749, 64-A; (c) Y 000593, 127-A; (d) Y 000749, 72-A; (e) Y 000802, 36-A; (f) crystal shape long axis diameter of all crystals with axis parallel (±5°) to the plane of the analyzed section.

Augite Preferred Orientation

Inverse pole figure and Euler angles measured by EBSD provide crystal orientation (Fig. 1b; Table 4). A subset of crystals with at least one crystallographic axis oriented parallel to the map plane (±5°) was created to assess crystal shape more accurately (Table 4: elongate grains oriented in map plane). For the oriented subset, aspect ratios averaged 1.24 ± 0.2–2.62 ± 0.81 (Table 4). Considering crystals where the <c> axis (i.e., long shape-axis) is oriented parallel to the map plane, a larger discrepancy is observed in the aspect ratio (Table 4; aspect ratio C-axis) compared to considering the aspect ratio of all axes (Fig. 5f; Table 4; aspect ratio of all axes). The percentage of crystals with their <c> axis oriented in the section is low for all samples and ranges from 1.8 to 11.6 (Table 4; elongate grains

oriented in the section), where the smallest percentage occurs in Y 000593 (127-A) and the largest in Y 000802.

Augite SPO

EBSD data confirm coupling between the long shape axis and the crystallographic <001> axis in augite for all samples (Figs. 1b, 7a, and 7b). Therefore, the CPO of the crystallographic [001] axis can be utilized as a proxy for the long shape axis to assess orientation corrected SPO within the samples. For SPO analysis, only crystals ≥0.3 mm within the EBSD reduced OPPG subset were considered (Fig 7a). Aligned SPO was observed along 45–225° and 135–315° in sections Y 000749 (64-A) and Y 000802 (36-A), respectively. Two conflicting SPO orientations; one major SPO plus one or more minor SPO (i.e., weaker/secondary SPO) is observed within sections Y 000593 (106-A) and Y
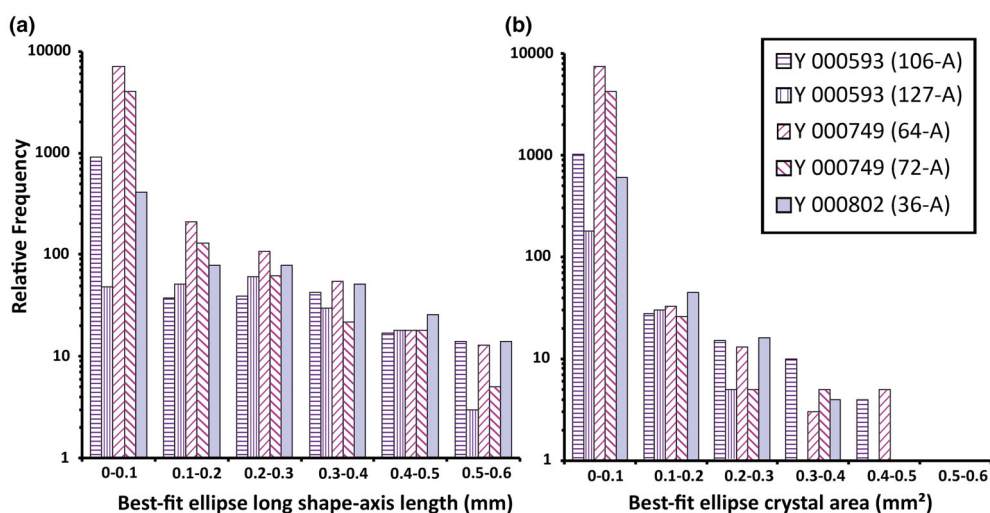
Fig. 6. EBSD derived augite size. a) Crystal size determined from the <c> axis length, which corresponds to the crystal's long shape axis corrected for crystal orientation (summarized for crystals ≥0.3 mm in Table 4). b) Crystal area as calculated using HKL Channel 5's best-fit ellipse algorithm. Relative frequency of both parameters is plotted on a log scale.

000593 (127-A; Fig. 7a). Section Y 000749 (72-A) exhibits two potential competing SPOs at ~90° to each other around 90–270° and 15–195°, with the 90–270° SPO appearing slightly more dominant. IPF data (Fig. 1b) visually confirm the presence of two crystal alignments within both Y 000593 sections and Y 000749 (64-A)'s map plane.

Augite CPO

Intercrystalline CPO using the reduced OPPG EBSD data set (Table 4: n_{OPPG} is plotted in Fig. 7b). However, CPO index calculations were assessed using the MTEX derived data set (n_{MTEX}, Table 4) which calculated a higher number of crystals within the EBSD data sets. For the CPO index calculations, only Y 000593 (106-A) was calculated from <300 crystals and as such is associated with a slightly higher analytical uncertainty (Table 4: n_{MTEX}). M-index indicates random CPO for all samples (Table 4). Y 000749 exhibiting the highest index value (0.04), followed by Y 000593 (0.03), with Y 000802 exhibiting the lowest (0.02). J-Index values correspond to medium strength CPO, typically observed in plutonic rocks. The highest J-index value of 4.76 ± 0.23 is in Y 000593 (127-A) and lowest value of 2.72 ± 0.14 in Y 000802 (36-A; Table 4). The averaged J-index values for Y 000593 and Y 000749 sit outside analytical uncertainty, where Y 000593 exhibits an overall stronger averaged medium alignment (4.10 ± 0.21) than Y 000749 (3.19 ± 0.16; Table 4).

Eigenvalue analysis of CPO (summarized in Table 4 and plotted in Fig. 8) identifies the presence of a low-intensity weak–moderate [001] girdle CPO in all

sections ($G_{001} = 0.19$–0.44; Fig. 8; Table 4). A significant discrepancy between the CPO strengths is observed within the two Y 000593 samples ($G_{001} = 0.27$ and 0.41; Figs. 7b and 8) indicating both a weak and moderate strength CPO for the meteorite. Weak strength point CPO (P_{100} Y 000749 and Y 000802 and P_{010} Y 000593) which are overshadowed by the more dominant G_{001} CPO are also observed (Figs. 7b and 8; Table 4). LS-Index results indicate foliation (Pure G_{100}) "S-type" CPO to a combined lineation (P_{010})–foliation (G_{001}) "LS-type" CPO (0.28–0.54) for all samples (Table 4). BA-index results indicate lineation (P_{010}) "B-type" CPO for Y 00593 (0.29 [106-A] and 0.36 [127-A]), foliation (G_{100}) "A-type" CPO for Y 000749 (0.58 [64-A] and 0.81 [72-A]), and combined lineation (P_{010})–foliation (G_{100}) "BA-type" CPO for Y 000802 (0.41; Table 4).

Intracrystalline misorientation patterns (Fig. 7c) can be used to indirectly assess slip systems. Sample referenced misorientation patterns indicate directional strain across all the Yamato meteorites. The observed misorientation patterns in the crystal reference frame relate to the following dominant slip systems expressed as either (001)[100]:(100)[001] in Y 000593 (both sections) and Y 000802 and {110}<001> or {110}$^{1}/_{2}$<110> in both Y 000749 sections.

Augite Spatial Distribution

New SDP analyses were conducted for the Yamato nakhlite sections Y 000593 (127-A), Y 000749 (64-A), and Y 000802 (36-A) (CSD data set). R-values, which
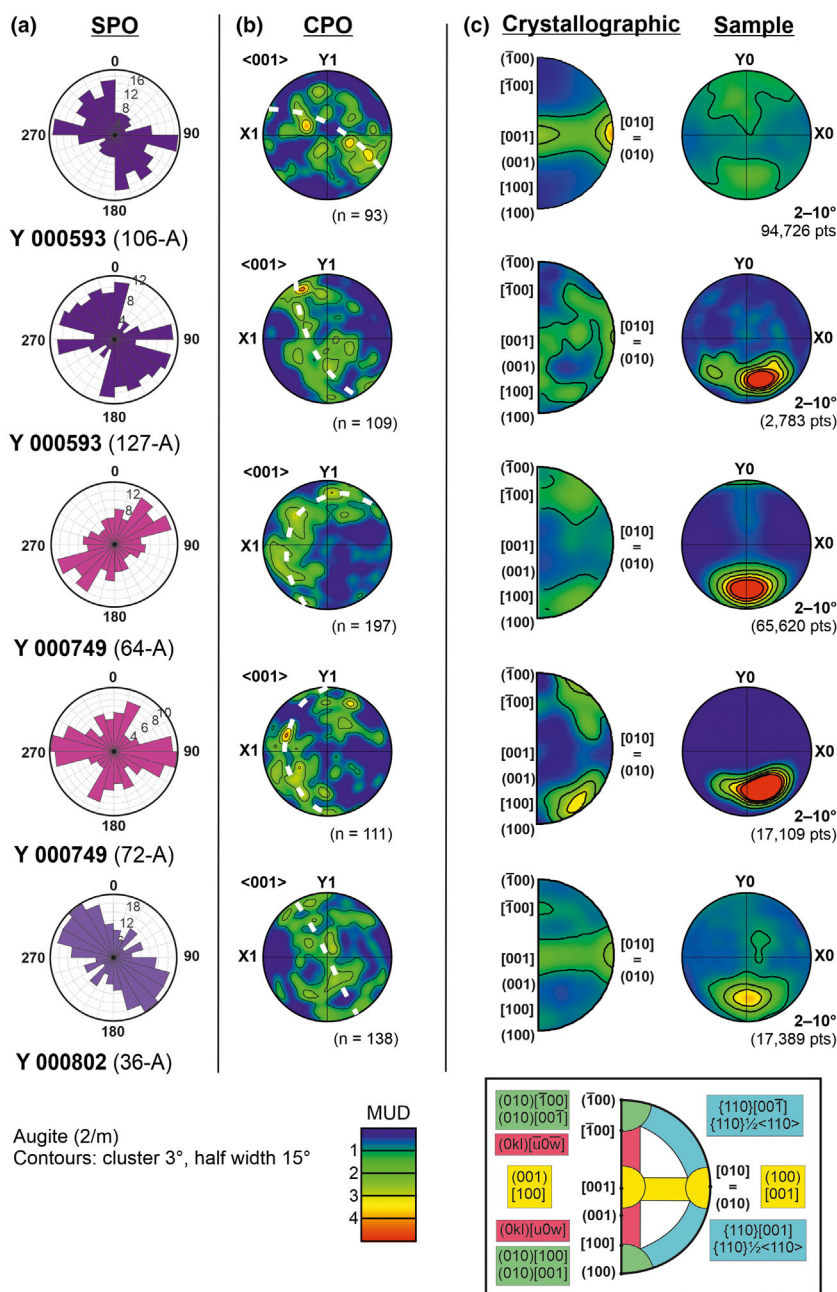
Fig. 7. EBSD augite intercrystalline and intracrystalline orientations. a) Shape preferred orientation (SPO) from one point per grain (OPPG) data, where SPO is determined from the 2-D long axis of fitted ellipse slope angle of grains ≥0.3 mm. b) Equal area, lower hemisphere stereographic projection (pole figure) for <100> axis of OPPG crystals ≥0.3 mm, where n refers to n_{OPPG} (EBSD data set; Table 4). All samples exhibit a <c> axis girdle (i.e., foliation) crystal preferred orientation (CPO) indicated by the white dashed lines. Quantitative results from further MTEX CPO analysis are in Table 4. c) Intracrystalline misorientation 2–10° in both crystal (semicircle) and sample (circle) reference frames. Shifts between the type of misorientation are observed in the crystal reference plots (left) indicating different external stress/strain conditions for each stone. Point maxima shown in the sample reference plots (right) reveal directional strain indicating a noncumulate formation mechanism. For additional CPO plots, the reader is referred to Appendix S1.

reflect the degree of crystal ordering, range from 1.39 to 1.44, while melt percent values range from 29.7% to 33.4% (Table 2). These new SDP results fall within the touching crystal framework region (Fig. 9). SDP results for samples Y 000593 (106-A) and Y 000749 (72-A) are reported in Udry and Day (2018).
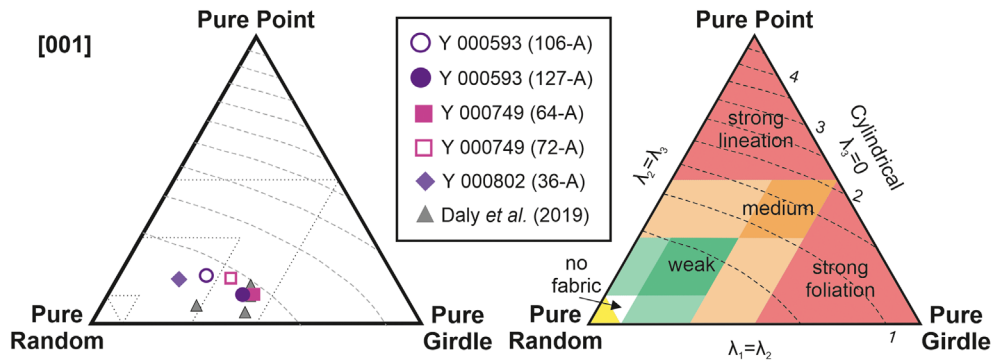
Fig. 8. Ternary plot of augite [c] axes in Yamato nakhlites determined using EBSD Eigenvalues; pure random (R), pure point (P), and pure girdle (G) maxima (EBSD data set Table 4). Differences in CPO strength and type between the two Y 000593 samples may be an artifact of separation within the meteorite from where each thick section was cut, or an example of the meteorite's heterogeneity.
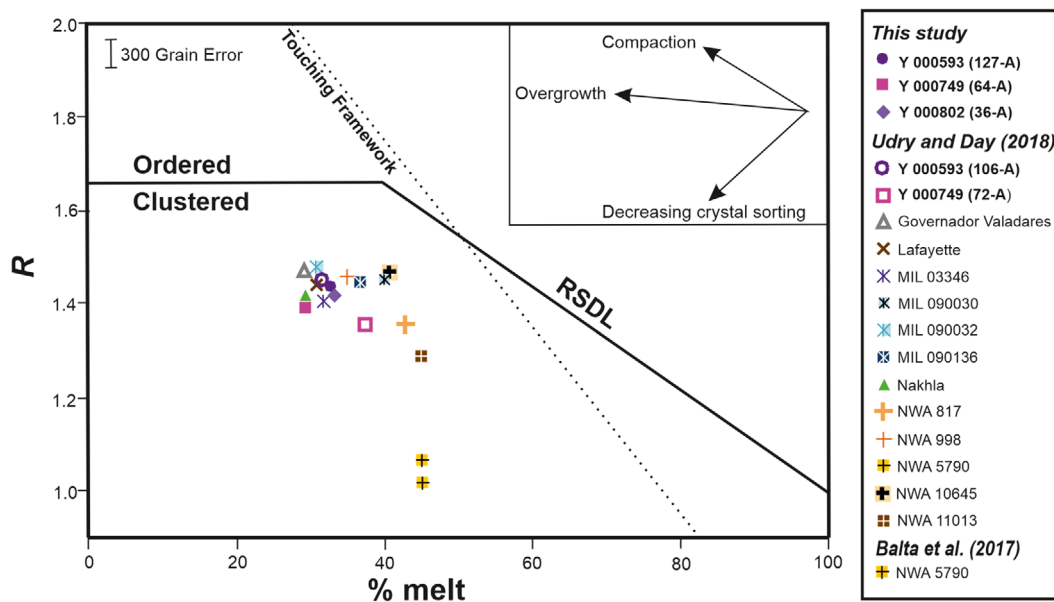

Fig. 9. Spatial distribution pattern (SDP) analysis of augite within the Yamato nakhlites (CSD data set, Table 2), where the % melt is plotted against the R-value (the ratio between the predicted and measured grain center from the 2-D CSD data set). Results from the present study are consistent with those reported by Balta et al. (2017) and Udry and Day (2018). RSDL—random sphere distribution line.

Augite Residence and Crystallization

Magma chamber residence times were calculated for Y 000593 (127-A), Y 000749 (64-A), and Y 000802 (36-A) using phenocryst populations ≥0.3 mm from the CSD data set. Results for sections Y 000593 (106-A) and Y 000749 (72-A) are reported in Udry and Day (2018). Calculations using the clinopyroxene-specific growth rate of Leu (2010) yielded residence times of 88 ± 4 yr for Y 000593 (127-A), 88 ± 6 yr for Y 000802 (36-A), and 105 ± 4 yr for Y 000749 (64-A; Table 3). In contrast, calculations using the growth rates of Cashman and Marsh (1988) and Jerram (2003)

resulted in residence times of 9 yr for Y 000593 (127-A) and Y 000802 and 10 yr for Y 000749 (64-A; Table 3).

The CSD slope and intercept reflect a given sample's crystallization/cooling rate. Slopes generated from sections Y 000593 (127-A), Y 000749 (64-A), and Y 000802 (36-A; this study) range from -2.9 ± 0.12 mm^{-1} to -3.45 ± 0.14 mm^{-1}, with their associated CSD slope intercepts ranging from 4.04 ± 0.11 to 4.43 ± 0.2 (Table 3). Note that Y 000749 (64-A) exhibits an anomalous decrease at 0.5 mm crystal size, which is not seen in the section Y 000749 (72-A) analyzed by Udry and Day (2018).

DISCUSSION

Strengths of CSD and EBSD Techniques

CSD and EBSD are powerful quantitative textural techniques (Cashman & Marsh, 1988; Marsh, 1988; Prior et al., 1999, 2009; Zieg & Marsh, 2002), each of which can answer different microstructural questions. However, for the most studies on achondrite meteorites, only CSD or EBSD is used. The application of multiple quantitative techniques enables a more robust investigation and understanding as the collected data are scrutinized from more than one point of view. This enhanced perspective in turn provides greater reliability and dimension to the derived interpretations, as illustrated by the Yamato nakhlite petrogenesis presented here.

Both EBSD and CSD analyses derive their data from a 2-D surface plane where the results are interpreted using multiple lines of evidence. In the case of EBSD, the data are derived from crystal lattice plane diffraction patterns (Kikuchi patterns). Once processed, these patterns are typically assessed via a series of images (e.g., Fig. 1) where the spatial resolution of the data is determined by the analysis step size (Halfpenny, 2010; Prior et al., 2009). EDS maps are often acquired in parallel to check for pattern mis-indexing. For larger stitched-area EBSD maps (e.g., Fig. 1), machine and beam drift can impact the detected crystal sizes and panel overlap, and if not treated properly can introduce artifacts (Halfpenny, 2010). CSD data sets are manually produced. The manual creation of the map means that the derived data are operator specific. For the present study, multiple different petrographic images (including those produced from EBSD and EDS analysis) were consulted in conjunction with optical assessment to produce the CSD data set (Fig. 2). A single operator (AU) conducted analyses for all CSD images to reduce operator bias between data sets; however, as with any manual analysis, an element of user bias will still be present.

Typically, 2-D polished sections that are used for microstructural analysis are prepared perpendicular to the structure of interest, or at least to a known external reference. However, sections made from samples which lack their emplacement context (e.g., meteorites) require crystal orientation to be corrected prior to any interpretation. EBSD excels in detecting crystal orientation (Prior et al., 2009). The technique leverages the position of each crystallographic axis to access the third dimension of a crystal relative to the 2-D analysis plane, as reported as via IPF or Euler data. These IPF/Euler EBSD data can assist in correcting CSD data sets which traditionally apply assumed crystal habits to reorient user-inputted crystal aspect ratios using the software CSDcorrections (Higgins, 2000).

Crystal shape is intrinsically linked to the crystallographic axis, where the shortest crystallographic axis typically relates to the long shape axis. Identification of the corresponding axes (e.g., <001> for augite) enables EBSD to identify and constrain preferred orientations that are not obviously aligned in the section. In the case of the Yamato nakhlites, the EBSD identified preferred orientation is of a low intensity and weak–moderate strength, where the section is not ideally oriented with respect to the SPO. These factors mean that SPO is difficult to identify in the 2-D plane without leveraging CPO. Thus, even though CSD can be used to identify SPO in samples, EBSD would be the recommended technique for SPO identification in achondrite meteorites.

Assessment of crystal growth and magma residence times requires an accurate determination of a crystal's shape (aspect ratio, width, and length), and CSD is the recommended technique. CSD is highly user-dependent, and relying on the experience of the user can be considered an advantage or disadvantage when it comes to determining grain boundaries. Using CSD, crystal boundaries are identified from multiple lines of evidence, whereas EBSD uses computational algorithms based off diffraction patterns and user-inputted misorientations. Thus, EBSD-reported crystal sizes will often be smaller than those measured using CSD due to the loss of diffraction pattern quality along the edges of crystals, and the misidentification of fractured crystallites as individual crystals (hence the use of a reduced OPPG data set used here). These constraints would ultimately result in crystal growth rates and magma chamber residence times being less accurate.

Both EBSD and CSD are modern quantitative techniques. The present study, which revisits the petrogenesis of the Yamato nakhlites, shows how each technique can aid and enhance data collection and interpretation from the other. Although both techniques have their strengths and weaknesses, when their data are combined and assessed together, the physical processes recorded within the Yamato nakhlites can be more accurately quantified.

Petrogenesis of the Yamato Nakhlites

The Yamato nakhlites are mafic augite-rich rocks (Imae et al., 2005; Misawa et al., 2003; Udry & Day, 2018). Initial discussions of their petrogenesis considered the three individual Yamato nakhlite stones as paired fragments derived from a larger nakhlite source cumulate pile on Mars (Imae et al., 2005; Misawa et al., 2003). However, the identification of new nakhlites since the Yamato nakhlites were recovered in 2000, together with higher resolution dating by Cohen et al. (2017), has shown that the nakhlites represent

multiple igneous bodies sourced from a more diverse environment than initially hypothesized (Day et al., 2018; Jambon et al., 2016; Krämer Ruggio et al., 2020; Treiman & Irving, 2008; Udry & Day, 2018; Udry et al., 2020). The CSD and EBSD data for all three Yamato nakhlites that are presented below are discussed and compared against previously reported petrological results (e.g., Corrigan et al., 2015; Imae et al., 2005; Udry & Day, 2018). The discussion below is in four parts: (i) SDP of the crystals within the Yamato nakhlites are discussed to assess the formation processes; (ii) the crystal growth rates of augite via CSD are assessed to interpret magma chamber residence and the impact on emplacement microstructures; (iii) the identified SPO and CPO are discussed; (iv) all the results are compiled to build a picture of the petrogenesis of the Yamato nakhlites.

Constraining Augite Formation Processes from Spatial Distribution Patterns

The SDP results from CSD analysis are in agreement with previous investigations of nakhlite CSD (Imae et al., 2005; Udry & Day, 2018). They are also consistent with SDP observations from other achondrite meteorites such as lunar basalts (Donohue & Neal, 2015). Four of the five data sets exhibit crystal ordering within a similar clustered region (Fig. 9), indicating an igneous source where the augite mostly grew in the magma chamber prior to emplacement (Fig. 9). Crystal frameworks, or clustered crystals, are structures typically associated with cumulates (Jerram, 2003; Jerram et al., 1996; Tegner et al., 2009). However, on Earth, cumulate-type descriptions can be associated with other igneous-type bodies, but rarely with surficial flows as the latter produce ordered phenocryst SPO (Hunter, 1996; Jerram et al., 1996; Rudge et al., 2008).

Differences in SDP results are observed between the two Y 000749 sections (Fig. 9). Even within the same igneous body standard igneous processes, for example, mechanical compaction, have been observed to result in variations in crystal ordering (Jerram et al., 1996, 2018). In the case of Y 000749, the disparity arises from contrasting calculated melt fractions resulting in a slightly lower ordering of crystals in Y 000749 (64-A; Table 2). This lower calculated melt fraction indicates heterogeneity in Y 000749, where the difference in melt fraction sits within the variation parameters typically observed between sections made from the same nakhlite stone (Corrigan et al., 2015). The average crystal size, crystal distribution, and crystal aspect ratios reported here for Yamato nakhlites indicate a similar formation process and mechanism for all three stones, albeit with some subtle differences accounting for sample heterogeneity (Figs. 3 and 6; Table 3).

Augite Growth and Magma Chamber Residence Time

Residence times calculated for augite are dependent on the CSD measured slope and intercept generated from crystal population density versus crystal size (Fig. 3; Table 3). The Yamato nakhlite magma chamber residence times calculated using the silicate growth rates of Cashman and Marsh (1988) and Jerram (2003) differ by up to 3 yr (9–12 yr; Table 3) and are similar to those calculated by Udry and Day (2018). Growth calculations using the clinopyroxene-specific growth rate of Leu (2010) imply longer residence times for all samples differing up to 29 yr. Y 000593 (127-A) and Y 000802 (36-A) have the shortest residence times (88 ± 4 and 88 ± 6 yr, respectively), that sit outside the analytical uncertainty of Y 000749 (64-A; 105 ± 4 yr; Table 3) and previously reported ages (117 yr Y 000593 [106-A] and 112 yr Y 000749 [72-A]; Udry & Day, 2018).

Note that these calculations assume that the augite crystals were growing continuously without interruptions and so represent minimum magma chamber residence times. Y 000593 exhibits the largest residence time range, encompassing the calculated ages of the other two stones (Table 3). The two clinopyroxene ages reported for Y 000593 sit outside analytical uncertainty, indicating heterogeneity within the stone. This heterogeneity could indicate convection within the nakhlite magmatic chamber, slight crystal settling during emplacement, potential recrystallization within part of the Y 000593 meteorite, or even that the meteorite contains a boundary between volcanic units or an inclusion.

In thicker flows, sills, and dykes, the rate of heat dissipation will often vary as a function of the external temperature and mechanical pressures (Goode, 1976; Iezzi & Ventura, 2002; Settle, 1979). Parts of the igneous body that retain heat longer due to insulating properties would enable coarser phenocrysts to grow and a crystalline (rather than glassy) mesostasis material to develop, thus increasing the calculated residence age (Hunter, 1996). This type of mechanism would agree with calculated growth rates from Cashman and Marsh (1988) and Jerram (2003), and with the Yamato nakhlites forming as a single unit. This mechanism would even explain the 7-yr Leu (2010) Y 000749 (64-A and 72-A) calculated residence time difference if the igneous body was plutonic, but not the Y 000593 (106-A and 127-A) 29-yr Leu (2010) calculated difference, or the crystallization age discrepancy reported by Cohen et al. (2017) between the different stones. As it is a 13.7 kg rock (Misawa et al., 2003), the difference in crystal residence times between different samples of Y 000593 would require a fairly localized mechanism, for example, chilled margin of a sill, dyke, base of a lava flow, slower heat dissipation from localized clusters or mushes, or shock induced melting (Holness et al., 2017;

Jerram, 2003; Jerram et al., 1996; Smith, 2002; Zieg & Marsh, 2002). Results from the intracrystalline misorientation patterns (Fig. 7c) suggest crystal annealing/partial recrystallization within Y 000593 (127-A) as the most likely explanation for heterogeneity in the residence time.

Previous investigations of several different nakhlites, including the Yamato nakhlites, have found evidence for dissolution in olivine phenocrysts ≥4 mm (Imae et al., 2005; Krämer Ruggio et al., 2020; Treiman, 2005). Chemical and size discrepancies within nakhlite olivines indicate at least two growth events or noncontinuous growth of the mineral, where the smaller crystals are currently to have crystallized post-augite (Treiman, 2005). Although olivine data are not being discussed in this paper, the possibility of augite dissolution needs to be considered as the process would impact calculated residence times and interpretations of CSD data. Crystals with long shape axis lengths ≥4 mm were detected by CSD but not EBSD. The discrepancy in identified long shape axis ≥4 mm crystals is most likely related to grain boundary determination in the EBSD data set. Petrological investigation of the larger augite crystals revealed no signs of dissolution. However, an anomalous dip in the frequency of 0.4 mm-sized crystals was observed in Y 000749 (64-A; Fig. 3, CSD data set). When assessed against the EBSD data set, no anomaly is observed in the corresponding crystal-shape length data (Fig. 6a). A dip is observed though, in the EBSD frequency of crystal area sizes in the range of 0.3–0.4 mm^2 for Y 000749 (64-A; Fig. 6b). Assessment of Y 000749 (64-A)'s CSD frequency anomaly against its companion EBSD data set in conjunction with no anomaly being observed in Y 000749 (72-A) indicates the frequency anomaly to be related to introduced sampling bias in the section, most likely linked to cutting artifacts. Lack of evidence for dissolution of augite in conjunction with measured crystal size distributions (both data sets) and previously determined chemical compositions (Imae et al., 2005; Treiman, 2005; Udry & Day, 2018) indicate homogenous uninterrupted growth from a single evolved unmixed magma source for augite in all samples.

Intracrystalline misorientation patterns from the EBSD data set agree with Y 000593 and Y 000749 forming as different units. The patterns indicate external stress/strain conditions that could not be resolved from fragments of the same parent rock: high-temperature/low-pressure conditions for Y 000749 (Ingrin et al., 1991; Kollé & Blacic, 1983) and moderate temperature/moderate pressure for both Y 000593 and Y 000802 (Avé Lallemant, 1978; Kollé & Blacic, 1982, 1983). Signatures within Y 000593 (127-A) indicate creep deformation within the augite that could be related to a partial recrystallization or an annealing event within the

section that is not observed in Y 000593 (106-A; Fig. 7c). This could quite easily be related to a localized event such as heating from hypervelocity impact or from a neighboring intrusion, which would result in a lower localized calculated residence age for the section.

Quantifying Igneous Microstructures from Preferred Orientation

Augite crystals within the Yamato nakhlites are euhedral with a defined long shape axis. Crystals that form habits with a defined long shape axis typically become aligned in response to increased internal strain (Bhattacharyya, 1966). However, variable SPO is common throughout all studied igneous bodies (Chin et al., 2020; Piazolo et al., 2002; Shelley, 1988) where the development of SPO can be disrupted by minor phases or even smaller crystals within the igneous body (Piazolo et al., 2002). In the case of highly crystalline melts (e.g., cumulates), lack of melt may also hinder SPO development (Hunter, 1996). Representative SPO analysis requires a statistically relevant number of crystals to be assessed. However, statistically relevant data sets are not always attainable for meteorite studies due to limited sample availability coupled with generally lower intensity crystal orientations. Crystal fracturing, often related to shock deformation, is a common feature within meteorites that can bias SPO results if not properly accounted for (Leroux, 2001).

SPO is a 3-D feature but has traditionally been identified using 2-D analysis. The reference frame of the section relative to the inherent SPO is a vital component that impacts the visibility of SPO. A good example is the consistent visible [001] girdle CPO (Fig. 7b) but variable SPO (Fig. 7a) results for the Yamato nakhlites. For meteorites and some types of terrestrial plutonic samples, lack of an initial knowledge relating the analysis surface to any SPO present requires additional analyses such as CPO to be undertaken. CPO assesses each crystal orientation with respect to rotation of the crystallographic axis. This is particularly useful when comparing preferred orientation across multiple samples, as the crystallographic axis is used as a consistent reference frame removing bias from the lack of geological context between each stone and/or section as well as any bias between the analyzed surface and the inherent SPO.

SPO and CPO within fine-grained mafic rocks, such as the Yamato nakhlites, can be difficult to identify even in terrestrial samples. The use of techniques such as EBSD CPO enables quantified identification of weaker and lower intensity SPO. Despite Figure 7b showing an identifiable girdle CPO across all Yamato nakhlite sections, neither the strength of the CPO nor its intensity can be quantified from the presented pole figure. Each of the three metrics used to quantify the identified CPO (M-index, J-index, and Eigenvalue analysis) impart subtly different information

that when assessed in combination can provide a better characterization of CPO.

EBSD-calculated quantitative CPO metrics confirms the presence of a comparable low-intensity weak–moderate strength [001] axis girdle CPO (i.e., foliation—alignment of the [001] axis within a singular plane) for all three Yamato nakhlite stones (Fig. 7b; Table 4). Girdle CPO is consistent with crystal settling SPO commonly observed in sills, lava lakes, and larger volume lava flows (Daly, Piazolo, et al., 2019; Iezzi & Ventura, 2002; Piazolo et al., 2002). The development of girdle CPO is also common for cumulate-like rocks (Hunter, 1996). However, the identified girdle CPO is coupled with a low-intensity weak point CPO (i.e., lineation—alignment in a given direction) within either the [100] or [010] axis indicating two or more strain fields acting on the sample evidencing a lesser component of flow in all samples (Table 4; Bertolett et al., 2019; Daly, Piazolo, et al., 2019; Prior et al., 1999). This presence of the weaker lineation CPO is supported by the sample referenced intracrystalline misorientation patterns (Fig. 7c), which show directional strain within all of the sections that is evidence for noncumulate formation.

The observed shift between [100] and [010] point CPO indicates different strain forces being recorded within Y 000593 compared to Y 000749 and Y 000802 (Table 4). Different external strain conditions between Y 000593 and Y 00749 are also observed in the intracrystalline misorientation patterns (crystal reference Fig. 7c); however, in this instance, Y 000802 indicates patterns consistent with Y 000593. Thus, the combined intercrystalline and intracrystalline CPO agree with Cohen et al. (2017) for the Yamato nakhlites to be considered as separate nakhlite units rather than parts of the same unit. However, depending on the original thickness of the emplaced layer, the stones could still potentially be considered as being fall-paired.

Comparison of SPO and CPO results for the replicate Yamato nakhlite sections highlights that although the identification of 2-D SPO within a sample is important for assessing microstructures, common reference frames are required for accurate SPO interpretations. Due to the random cut of each section and lack of external geological context, it is recommended that the identification of microstructures for achondritic meteorites, such as the Yamato nakhlites, should be made considering both 2-D SPO and CPO analyses.

Emplacement of the Yamato Nakhlites

Variation in CPO and SPO strength within the same igneous body is fairly common within terrestrial sills, dykes, or large surficial lava flows (Iezzi & Ventura, 2002). In these types of contexts, flow microstructures are observed to be stronger along the margins of the igneous body compared to the center. Subflows occurring in the opposite direction to the dominant flow direction are also common features within igneous bodies. These opposing flow SPO and CPO can in turn influence the strength and order of any detected microstructures (Iezzi & Ventura, 2002; Ildefonse et al., 1992; Shelley, 1985). Geological samples (particularly from low-viscosity magmas) typically have significant heterogeneity (Higgins, 2006; Nolze, 2005; Vetere et al., 2019; Winter, 2013). Considerable changes in SPO and CPO within a relatively short distance, that is, within a single sample, are not uncommon. In terms of Martian meteorites, visible SPO and CPO heterogeneity has only been reported for shergottites Zagami (Becker, 2011) and Allan Hills (ALH) 77005 (Ikeda, 1994). Although both examples above are sourced from different regions on Mars than the nakhlites, they indicate that variability is also characteristic of Martian magmas.

When all the microstructural information is compiled and considered for both CSD and EBSD analyses, the following quantitative description of the Yamato nakhlites' petrogenesis can be derived. Relative to other nakhlite samples, augite crystals in the Yamato nakhlites grew slowly in a magma chamber, with minimum residence times of either 9–12 yr or 88–117 ± 6 yr (Fig. 4) (Udry & Day, 2018). The magma (with augite phenocrysts) was then brought toward/close to the planet's surface, where the phenocrysts continued to grow as indicated by their augite rims. External stress/strain conditions during the Yamato nakhlites' emplacement on Mars resulted in low-intensity SPO and dominant girdle CPO (foliation) along the <001> axis with a minor point (lineation) component along the [100] axis for Y 000749 and Y 000802, and [010] axis for Y 000593 (Table 4). Assessment of intercrystalline CPO using the three quantitative metrics reveals subtle differences between the different meteorite stones. These CPO results when assessed individually often show as a continuum between the samples. However, when assessed in combination, the relationship between the stones appears to be more random. Assessment of the intracrystalline misorientation CPO patterns of augite across all stones shows evidence of directional strain implying a component of flow during emplacement (Fig. 7c), where intracrystalline misorientation CPO patterns show Y 000749 to have undergone higher temperature stress/strain conditions than Y 000593 and Y 000802.

In summary, the data presented suggest the following series of geological events during the Yamato nakhlite's emplacement: (i) Augite phenocrysts grew in the nakhlite magma chamber for either 9–12 or 88–117 yr, which are longer magma chamber residence times than other analyzed nakhlites (Udry & Day, 2018); (ii) magma was transported from the magma chamber and either erupted

at the surface only to pool as a low viscosity lava or was injected into the crust as a shallow sill. During emplacement cooling, the Yamato nakhlites crystallized in a clustered touching framework; (iii) during cooling of the magma body, all stones formed microstructures relative to a dominant planar external strain (most likely gravity) with minor directional strain (indicating a component of flow), for example, from gravitational settling within a noncumulate stagnant magma body, as indicated by the observed [001] girdle CPO, LS, and BA index values, and the directional, sample-referenced, intracrystalline misorientation patterns. The combination of information from CPO, SPO, CSD, SDP, and crystal residence times indicates that the Yamato nakhlites formed as separate bodies within a similar magmatic regime and most likely as a series of shallow sills or different lobes at the edge of a stagnant lava pond or lake.

CONCLUSIONS

CSD (including CSD and SDP analyses) and EBSD are quantitative analytical techniques that excel in different aspects of microstructural measurement and answer different fundamental questions pertaining to the petrogenesis and evolution of a given sample. Comparison of these techniques shows that CSD is best used to assess crystal growth and magmatic residence times, whereas EBSD is most effective for quantifying features such as those produced by magmatic flow or crystal settling.

Application of CSD and EBSD techniques to the Yamato nakhlites has enabled their petrogenesis to be further quantified and therefore better constrained. CSD-calculated magmatic residence times indicate that augite crystals in Yamato nakhlites spent either 9–12 or 88–117 ± 6 yr in the magma chamber. CSD analyses indicate that phenocrysts within these samples grew over a longer period than the overall nakhlite group. The magma and crystals were brought to (or near) the surface, where SDP analyses indicate that the Yamato nakhlites formed within a clustered touching framework. Finally, using EBSD, the presence of variable strength [001] axis girdle CPO is identified with a weak point CPO in one of the other crystallographic axes in each sample. Intracrystalline misorientation patterns indicate noncumulate formation strains in all samples, with differing external parameters for Y 000749 in comparison to Y 000593 and Y 000802 indicating formation as separate units. The reported CPO has been observed in low-viscosity terrestrial basaltic lavas, and sills, where crystal settling due to gravity is the dominant source of strain during emplacement. This study shows that quantitatively assessing SPO and CPO using multiple techniques in conjunction with each other can be used as a springboard for future analyses, particularly for achondrite meteorites from known planetary bodies (e.g.,

other Martian and lunar samples). Such work can provide more contextualized and comparable textural interpretations and results.

Data Availability Statement—The data that supports the findings of this study are available in the supplementary material of this article.

Editorial Handling—Dr. Akira Yamaguchi

REFERENCES

Avé Lallemant, H. G. 1978. Experimental Deformation of Diopside and Websterite. *Tectonophysics* 48: 1–27. https://doi.org/10.1016/0040-1951(78)90083-5.

Bachmann, F., Hielscher, R., and Schaeben, H. 2011. Grain Detection from 2d and 3d EBSD Data-Specification of the MTEX Algorithm. *Ultramicroscopy* 111: 1720–33. https://doi.org/10.1016/j.ultramic.2011.08.002.

Balta, J. B., Sanborn, M. E., Mayne, R. G., Wadhwa, M., McSween, H. Y., and Crossley, S. D. 2017. Northwest Africa 5790: A Previously Unsampled Portion of the Upper Part of the Nakhlite Pile. *Meteoritics & Planetary Science* 52: 36–59. https://doi.org/10.1111/maps.12744.

Barsdell, M. 1988. Petrology and Petrogenesis of Clinopyroxene-Rich Tholeiitic Lavas, Merelava Volcano, Vanuatu. *Journal of Petrology* 29: 927–64. https://doi.org/10.1093/petrology/29.5.927.

Becker, T. E. 2011. *Preferred Orientations of Pyroxene in the Zagami Shergottite: Implications for Magmatic Emplacement*. Colby College.

Bertolett, E. M., Prior, D. J., Gravley, D. M., Hampton, S. J., and Kennedy, B. M. 2019. Compacted Cumulates Revealed by Electron Backscatter Diffraction Analysis of Plutonic Lithics. *Geology* 47: 445–8. https://doi.org/10.1130/G45616.1.

Bestmann, M., and Prior, D. J. 2003. Intragranular Dynamic Recrystallization in Naturally Deformed Calcite Marble: Diffusion Accommodated Grain Boundary Sliding as a Result of Subgrain Rotation Recrystallization. *Journal of Structural Geology* 25: 1597–613. https://doi.org/10.1016/S0191-8141(03)00006-3.

Bhattacharyya, D. S. 1966. Orientation of Mineral Lineation Along the Flow Direction in Rocks. *Tectonophysics* 3: 29–33. https://doi.org/10.1016/0040-1951(66)90023-0.

Blamey, N. J. F., Parnell, J., McMahon, S., Mark, D. F., Tomkinson, T., Lee, M., Shivak, J., Izawa, M. R. M., Banerjee, N. R., and Flemming, R. L. 2015. Evidence for Methane in Martian Meteorites. *Nature Communications* 6: 7399. 10.1038/ncomms8399. http://www.nature.com/doifinder.

Boneh, Y., and Skemer, P. 2014. The Effect of Deformation History on the Evolution of Olivine CPO. *Earth and Planetary Science Letters* 406: 213–22. https://doi.org/10.1016/j.epsl.2014.09.018.

Borg, L. E., and Drake, M. J. 2005. A Review of Meteorite Evidence for the Timing of Magmatism and of Surface or Near-Surface Liquid Water on Mars. *Journal of Geophysical Research: Planets* 110: 1–10. https://doi.org/10.1029/2005JE002402.

Bunge, H.-J. 1982. Chapter 4 Expansion of Orientation Distribution Functions in a Series of Generalised Spherical Harmonics (Three-Dimensional Textures). In *Texture Analysis in Materials Science: Mathematical Methods*, edited by H.-J. Bunge, 47–118. Gottingen: Cuvillier Verlag.

Carr, M. H., and Head, J. W. 2010. Geologic History of Mars. *Earth and Planetary Science Letters* 294: 185–203. https://doi.org/10.1016/j.epsl.2009.06.042.

Cashman, K. V., and Marsh, B. D. 1988. Crystal Size Distribution (CSD) in Rocks and the Kinetics and Dynamics of Crystallization II: Makaopuhi Lava Lake. *Contributions to Mineralogy and Petrology* 99: 292–305. https://doi.org/10.1007/BF00375363.

Chin, E. J., Soustelle, V., and Liu, Y. 2020. An SPO-Induced CPO in Composite Mantle Xenoliths Correlated with Increasing Melt-Rock Interaction. *Geochimica et Cosmochimica Acta* 278: 199–218. https://doi.org/10.1016/j.gca.2019.10.002.

Cohen, B. E., Mark, D. F., Cassata, W. S., Lee, M. R., Tomkinson, T., and Smith, C. L. 2017. Taking the Pulse of Mars via Dating of a Plume-Fed Volcano. *Nature Communications* 8: 640. https://doi.org/10.1038/s41467-017-00513-8.

Corrigan, C. M., Velbel, M. A., and Vicenzi, E. P. 2015. Modal Abundances of Pyroxene, Olivine, and Mesostasis in Nakhlites: Heterogeneity, Variation, and Implications for Nakhlite Emplacement. *Meteoritics & Planetary Science* 50: 1497–511. https://doi.org/10.1111/maps.12492.

Daly, L., Lee, M. R., Piazolo, S., Griffin, S., Bazargan, M., Campanale, F., Chung, P., et al. 2019. Boom Boom Pow: Shock-Facilitated Aqueous Alteration and Evidence for Two Shock Events in the Martian Nakhlite Meteorites. *Science Advances* 5: 1–11. https://doi.org/10.1126/sciadv.aaw5549.

Daly, L., Piazolo, S., Lee, M. R., Griffin, S., Chung, P., Campanale, F., Cohen, B. E., et al. 2019. Understanding the Emplacement of Martian Volcanic Rocks Using Petrofabrics of the Nakhlite Meteorites. *Earth and Planetary Science Letters* 520: 220–30. https://doi.org/10.1016/j.epsl.2019.05.050.

Day, J. M. D., Tait, K. T., Udry, A., Moynier, F., Liu, Y., and Neal, C. R. 2018. Martian Magmatism from Plume Metasomatized Mantle. *Nature Communications* 9: 4799. https://doi.org/10.1038/s41467-018-07191-0.

Donohue, P. H., and Neal, C. R. 2015. Quantitative Textural Analysis of Ilmenite in Apollo 17 High-Titanium Mare Basalts. *Geochimica et Cosmochimica Acta* 149: 115–30. https://doi.org/10.1016/j.gca.2014.11.002.

Donohue, P. H., and Neal, C. R. 2018. Textural and Mineral Chemical Evidence for the Cumulate Origin and Evolution of High-Titanium Basalt Fragment 71597. *American Mineralogist* 103: 284–97. https://doi.org/10.2138/am-2018-6173.

Forman, L. V., Bland, P. A., Timms, N. E., Collins, G. S., Davison, T. M., Ciesla, F. J., Benedix, G. K., et al. 2016. Hidden Secrets of Deformation: Impact-Induced Compaction Within a CV Chondrite. *Earth and Planetary Science Letters* 452: 133–45. https://doi.org/10.1016/j.epsl.2016.07.050.

Forman, L. V., Timms, N. E., Bland, P. A., Daly, L., Benedix, G. K., and Trimby, P. W. 2019. A Morphologic and Crystallographic Comparison of CV Chondrite Matrices. *Meteoritics & Planetary Science* 2651: 2633–51. https://doi.org/10.1111/maps.13380.

Fritz, J., Artemieva, N. A., and Greshake, A. 2005. Ejection of Martian Meteorites. *Meteoritics & Planetary Science* 40: 1393–411. 10.1111/j.1945-5100.2005.tb00409.x.

Goode, A. D. T. 1976. Small Scale Primary Cumulus Igneous Layering in the Kalka Layered Intrusion, Giles Complex, Central Australia. *Journal of Petrology* 17: 379–97. https://doi.org/10.1093/petrology/17.3.379.

Greeley, R., and Spudis, P. D. 1981. Volcanism on Mars. *Reviews of Geophysics and Space Physics* 19: 13–41.

Grott, M., Baratoux, D., Hauber, E., Sautter, V., Mustard, J., Gasnault, O., Ruff, S. W., et al. 2013. Long-Term Evolution of the Martian Crust-Mantle System. *Space Science Reviews* 174: 49–111. https://doi.org/10.1007/s11214-012-9948-3.

Halfpenny, A. 2010. Some Important Practical Issues for the Collection and Manipulation of Electron Backscatter Diffraction (EBSD) Data from Geological Samples. *Journal of the Virtual Explorer* 35: 1–18. https://doi.org/10.3809/jvirtex.2011.00272.

Helmstaedt, H., Anderson, O. L., and Gavasci, A. T. 1972. Petrofabric Studies of Eclogite, Spinel-Websterite, and Spinel-Lherzolite Xenoliths from Kimberlite-Bearing Breccia Pipes in Southeastern Utah and Northeastern Arizona. *Journal of Geophysical Research* 77: 4350–65. https://doi.org/10.1029/JB077i023p04350.

Higgins, M. D. 2000. Measurement of Crystal Size Distributions. *American Mineralogist* 85: 1105–16. https://doi.org/10.2138/am-2000-8-901.

Higgins, M. D. 2006. *Quantitative Textural Measurements in Igneous and Metamorphic Petrology*. New York: Cambridge University Press.

Holness, M. B. 2007. Textural Immaturity of Cumulates as an Indicator of Magma Chamber Processes: Infiltration and Crystal Accumulation in the Rum Eastern Layered Intrusion. *Journal of the Geological Society* 164: 529–39. https://doi.org/10.1144/0016-76492006-021.

Holness, M. B., Nielsen, T. F. D., and Tegner, C. 2007. Textural Maturity of Cumulates: A Record of Chamber Filling, Liquidus Assemblage, Cooling Rate and Large-Scale Convection in Mafic Layered Intrusions. *Journal of Petrology* 48: 141–57. https://doi.org/10.1093/petrology/egl057.

Holness, M. B., Vukmanovic, Z., and Mariani, E. 2017. Assessing the Role of Compaction in the Formation of Adcumulates: A Microstructural Perspective. *Journal of Petrology* 58: 643–74. https://doi.org/10.1093/petrology/egx037.

Hunter, R. H. 1996. Texture Development in Cumulate Rocks. *Developments in Petrology* 15: 77–101. https://doi.org/10.1016/S0167-2894(96)80005-4.

Iezzi, G., and Ventura, G. 2002. Crystal Fabric Evolution in Lava Flows: Results from Numerical Simulations. *Earth and Planetary Science Letters* 200: 33–46. https://doi.org/10.1016/S0012-821X(02)00617-9.

Ikeda, Y. 1994. Petrography and Petrology of the ALH-77005 Shergottite. *Proceedings of the NIPR Symposium on Antarctic Meteorites* 7: 9–29. https://adsabs.harvard.edu/pdf/1994AMR....7....9I.

Ildefonse, B., Sokoutis, D., and Mancktelow, N. S. 1992. Mechanical Interactions Between Rigid Particles in a Deforming Ductile Matrix. Analogue Experiments in Simple Shear Flow. *Journal of Structural Geology* 14: 1253–66. https://doi.org/10.1016/0191-8141(92)90074-7.

Imae, N., Ikeda, Y., and Kojima, H. 2005. Petrology of the Yamato Nakhlites. *Meteoritics & Planetary Science* 40: 1581–98. https://doi.org/10.1111/j.1945-5100.2005.tb00133.x.

Imae, N., Ikeda, Y., Shinoda, K., Kojima, H., and Iwata, N. 2003. Yamato Nakhlites: Petrography and Mineralogy. *Antarctic Meteorite Research* 16: 13–33. https://adsabs.harvard.edu/pdf/2003AMR....16...13I.

Ingrin, J., Doukhan, N., and Doukhan, J. C. 1991. High-Temperature Deformation of Diopside Single-Crystal. 2. Transmission Electron-Microscopy Investigation of the Defect Microstructures. *Journal of Geophysical Research-Solid Earth and Planets* 96: 14287–97. https://doi.org/10.1029/91JB01233.

Ismaïl, W. B., and Mainprice, D. 1998. An olivine fabric database: An overview of upper mantle fabrics and seismic anisotropy. *Tectonophysics* 296: 145–57. https://doi.org/10.1016/S0040-1951(98)00141-3.

Jambon, A., Sautter, V., Barrat, J.-A., Gattacceca, J., Rochette, P., Boudouma, O., Badia, D., and Devouard, B. 2016. Northwest Africa 5790: Revisiting Nakhlite Petrogenesis. *Geochimica et Cosmochimica Acta* 190: 191–212. https://doi.org/10.1016/j.gca.2016.06.032.

Jerram, D. A. 2003. Quantifying the Building Blocks of Igneous Rocks: Are Clustered Crystal Frameworks the Foundation? *Journal of Petrology* 44: 2033–51. https://doi.org/10.1093/petrology/egg069.

Jerram, D. A., Cheadle, M. J., Hunter, R. H., and Elliott, M. T. 1996. The Spatial Distribution of Grains and Crystals in Rocks. *Contributions to Mineralogy and Petrology* 125: 60–74. https://doi.org/10.1007/s004100050206.

Jerram, D. A., Dobson, K. J., Morgan, D. J., and Pankhurst, M. J. 2018. The Petrogenesis of Magmatic Systems: Using Igneous Textures to Understand Magmatic Processes. In *Volcanic and Igneous Plumbing Systems: Understanding Magma Transport, Storage, and Evolution in the Earth's Crust*, edited by S. Burchardt, 191–229. Amsterdam, Netherlands: Elsevier. https://doi.org/10.1016/B978-0-12-809749-6/00008-X.

Kollé, J. J., and Blacic, J. D. 1982. Deformation of Single-Crystal Clinopyroxenes: 1. Mechanical Twinning in Diopside and Hedenbergite. *Journal of Geophysical Research* 87: 4019–34.

Kollé, J. J., and Blacic, J. D. 1983. Deformation of Single-Crystal Clinopyroxenes: 2. Dislocation-Controlled Flow Processes in Hedenbergite. *Journal of Geophysical Research* 88: 2381–93. https://doi.org/10.1029/JB088iB03p02381.

Korochantseva, E. V., Schwenzer, S. P., Buikin, A. I., Hopp, J., Ott, U., and Trieloff, M. 2011. ^{40}Ar-^{39}Ar and Cosmic-Ray Exposure Ages of Nakhlites-Nakhla, Lafayette, Governador Valadares-and Chassigny. *Meteoritics & Planetary Science* 46: 1397–417.

Krämer Ruggio, L., Gattacceca, J., Devouard, B., Udry, A., Debaille, V., Rochette, P., Lorand, J.-P., et al. 2020. Caleta el Cobre 022 Martian Meteorite: Increasing Nakhlite Diversity. *Meteoritics & Planetary Science* 25: 1–25. https://doi.org/10.1111/maps.13534.

Leroux, H. 2001. Microstructural Shock Signatures of Major Minerals in Meteorites. *European Journal of Mineralogy* 13: 253–72. https://doi.org/10.1127/0935-1221/01/0013-0253%0A.

Leu, A. R. 2010. Clinopyroxene Growth Rate in Mafic Melts. 2010 GSA Denver Annual Meeting, vol. 5: 100.

Longhi, J. 1991. Complex Magmatic Processes on Mars: Inferences from the SNC Meteorites (Abstract). 19th Lunar and Planetary Science Conference. pp. A91-42332 17–19. http://adsabs.harvard.edu/full/1991LPSC...21..695L

Mainprice, D., Bachmann, F., Hielscher, R., and Schaeben, H. 2015. Descriptive Tools for the Analysis of Texture Projects with Large Datasets Using MTEX: Strength, Symmetry and Components. *Geological Society Special Publication* 409: 251–71. https://doi.org/10.1144/SP409.8.

Marsh, B. D. 1988. Crystal Size Distribution (CSD) in Rocks and the Kinetics and Dynamics of Crystallization—I. Theory. *Contributions to Mineralogy and Petrology* 99: 277–91. https://doi.org/10.1007/BF00375362.

Marsh, B. D. 1998. Crystal Capture, Sorting, and Retention in Convecting Magma. *Special Paper of the Geological Society of America* 253: 399–416. https://doi.org/10.1130/0016-7606(1988)100%3C1720:CCSARI%3E2.3.CO;2.

McSween, H. Y. 1994. What We Have Learned About Mars from SNC Meteorites. *Meteoritics* 29: 757–79. https://doi.org/10.1111/j.1945-5100.1994.tb01092.x.

McSween, H. Y., and Treiman, A. H. 1998. Martian Meteroties. In *Planetary Materials. Reviews in Mineralogy*, edited by J. J. Papike, 1–53. Washington, D.C.: Mineralogical Society America.

Misawa, K., Kojima, H., Imae, N., and Nakamura, N. 2003. The Yamato Nahklite Consortium. *Antarctic Meteorite Research* 16: 1–12.

Morgan, D. J., and Jerram, D. A. 2006. On Estimating Crystal Shape for Crystal Size Distribution Analysis. *Journal of Volcanology and Geothermal Research* 154: 1–7. https://doi.org/10.1016/j.jvolgeores.2005.09.016%0A.

Morimoto, N., Fabries, J., Ferguson, A. K., Ginzburg, I. V., Ross, M., Seifert, F. A., Zussman, J., Aoki, K., and Gottardi, G. 1988. Petrology Nomenclature of Pyroxenes. *Reviews in Mineralogy* 39: 55–76. https://doi.org/10.1007/BF01226262.

Nolze, G. 2005. Application of Electron Back-Scatter Diffraction (EBSD) on Iron Meteorites. In *Microstructure Analysis in Materials Science*, edited by T. G. Fawcett, J. Faber, S. Kabekkodu, F. McClune, and D. Rafaja, 1–3. Freiberg: Freiberger Forschungshefte.

Nyquist, L. E., Bogard, D. D., Shih, C. Y., Greshake, A., Stöffler, D., and Eugster, O. 2001. Ages and Geologic Histories of Martian Meteorites. In *Chronology and Evolution of Mars. Space Sciences Series of ISSI*, edited by R. Kallenbach, J. Geiss, and W. K. Hartmann, 105–64. Dordrecht: Springer. https://doi.org/10.1007/978-94-017-1035-0_5.

Okazaki, R., Keisuke, N., Imae, N., and Kojima, H. 2003. Noble Gas Signatures of Antarctic Nakhlites, Yamato (Y) 000593, Y000749, and Y000802. *Antarctic Meteorite Research* 16: 58–79.

Paterson, S. R., Fowler, T. K., Schmidt, K. L., Yoshinobu, A. S., Yuan, E. S., and Miller, R. B. 1998. Interpreting Magmatic Fabric Patterns in Plutons. *Lithos* 44: 53–82. https://doi.org/10.1016/S0024-4937(98)00022-X.

Piazolo, S., Bons, P. D., and Passchier, C. W. 2002. The Influence of Matrix Rheology and Vorticity on Fabric Development of Populations of Rigid Objects During Plane Strain Deformation. *Tectonophysics* 351: 315–29. https://doi.org/10.1016/S0040-1951(02)00220-2%0A.

Prior, D. J., Boyle, A. P., Brenker, F., Cheadle, M. C., Day, A., Lopez, G., Peruzzi, L., et al. 1999. The Application of Electron Backscatter Diffraction and Orientation Constrast Imaging in the SEM to Textural Problems in Rocks. *American Mineralogist* 84: 1741–59. https://doi.org/10.1016/S0040-1951(02)00220-2%0A.

Prior, D. J., Mariani, E., and Wheeler, J. 2009. EBSD in the Earth Sciences: Applications, Common Practice and Challenges. In *Electron Backscatter Diffraction in Materials Science*, edited by A. J. Schwartz, M. Kumar, B. L. Adams, and D. P. Field, 2nd ed., 1–403. Boston, MA: Springer. https://doi.org/10.1007/978-0-387-88136-2_26.

Rahib, R. R., Udry, A., Howarth, G. H., Gross, J., Paquet, M., Combs, L. M., Laczniak, D. L., and Day, J. M. D. 2019. Mantle Source to Near-Surface Emplacement of Enriched and Intermediate Poikilitic Shergottites in Mars. *Geochimica et Cosmochimica Acta* 266: 463–96. https://doi.org/10.1016/j.gca.2019.07.034.

Rudge, J. F., Holness, M. B., and Smith, G. C. 2008. Quantitative Textural Analysis of Packings of Elongate Crystals. *Contributions to Mineralogy and Petrology* 156: 413–29.

Santos, A. R., Agee, C. B., McCubbin, F. M., Shearer, C. K., Burger, P. V., Tartèse, R., and Anand, M. 2015. Petrology of Igneous Clasts in Northwest Africa 7034: Implications for the Petrologic Diversity of the Martian Crust. *Geochimica et Cosmochimica Acta* 157: 56–85. https://doi.org/10.1016/j.gca.2015.02.023%0A.

Schneider, C. A., Rasband, W. S., and Eliceiri, K. W. 2012. NIH Image to ImageJ: 25 Years of Image Analysis. *Nature Methods* 9: 671–5. https://doi.org/10.1038/nmeth.2089.

Schwartz, A. J., Kumar, M., Adams, B. L., and Field, D. P. 2000. *Electron Backscatter Diffraction in Materials Science*, 2nd ed. Kluwer Academic, Plenum Publishers.

Settle, M. 1979. Lava Rheology: Thermal Buffering Produced by the Latent Heat of Crystallisation (Abstract). 10th Lunar and Planetary Science Conference. pp. 1107–9. http://adsabs.harvard.edu/full/1979LPI....10.1107 S.

Shearer, C. K., Burger, P. V., Papike, J. J., McCubbin, F. M., and Bell, A. S. 2015. Crystal Chemistry of Merrillite from Martian Meteorites: Mineralogical Recorders of Magmatic Processes and Planetary Differentiation. *Meteoritics & Planetary Science* 50: 649–73. https://doi.org/10.1111/maps.12355.

Shelley, D. 1985. Determining Paleo-Flow Directions from Groundmass Fabrics in the Lyttelton Radial Dykes, New Zealand. *Journal of Volcanology and Geothermal Research* 25: 69–79. https://doi.org/10.1016/0377-0273(85)90005-8%0A.

Shelley, D. 1988. Radial Dikes of Lyttelton Volcano—Their Structure, Form, and Petrography. *New Zealand Journal of Geology and Geophysics* 31: 65–75. https://doi.org/10.1080/00288306.1988.10417810.

Skemer, P., Katayama, I., Jiang, Z., and Karato, S. I. 2005. The Misorientation Index: Development of a New Method for Calculating the Strength of Lattice-Preferred Orientation. *Tectonophysics* 411: 157–67. https://doi.org/10.1016/j.tecto.2005.08.023%0A.

Smith, J. V. 2002. Structural Analysis of Flow-Related Textures in Lavas. *Earth-Science Reviews* 57: 279–97.

Taylor, G. J. 2013. The Bulk Composition of Mars. *Chemie der Erde—Geochemistry* 73: 401–20. https://doi.org/10.1016/j.chemer.2013.09.006.

Tegner, C., Thy, P., Holness, M. B., Jakobsen, J. K., and Lesher, C. E. 2009. Differentiation and Compaction in the Skaergaard Intrusion. *Journal of Petrology* 50: 813–40.

Tomkinson, T., Lee, M. R., Mark, D. F., Dobson, K. J., and Franchi, I. A. 2015. The Northwest Africa (NWA) 5790 Meteorite: A Mesostasis-Rich Nakhlite with Little or No Martian Aqueous Alteration. *Meteoritics & Planetary Science* 50: 287–304.

Treiman, A. H. 2005. The Nakhlite Meteorites: Augite-Rich Igneous Rocks from Mars. *Chemie der Erde—Geochemistry* 65: 203–70. https://doi.org/10.1016/j.chemer.2005.01.004%0A.

Treiman, A. H., and Irving, A. J. 2008. Petrology of Martian Meteorite Northwest Africa 998. *Meteoritics & Planetary Science* 43: 829–54. http://meteoritics.org.

Udry, A., and Day, J. M. D. 2018. 1.34 Billion-Year-Old Magmatism on Mars Evaluated from the Co-Genetic Nakhlite and Chassignite Meteorites. *Geochimica et Cosmochimica Acta* 238: 292–315. https://doi.org/10.1016/j.gca.2018.07.006.

Udry, A., Howarth, G. H., Herd, C., Day, J. M. D., Lapen, T. J., and Filiberto, J. 2020. What Martian Meteorites Reveal About the Interior and Surface of Mars. *Journal of Geophysical Research: Planets* 125: e2020JE006523. https://doi.org/10.1002/essoar.10503123.2.

Vetere, F., Murri, M., Alvaro, M., Domeneghetti, M. C., Rossi, S., Pisello, A., Perugini, D., and Holtz, F. 2019. Viscosity of Pyroxenite Melt and Its Evolution During Cooling. *Journal of Geophysical Research: Planets* 124: 1451–69.

Vollmer, F. W. 1990. An Application of Eigenvalue Methods to Structural Domain Analysis. *Bulletin of the Geological Society of America* 102: 786–91. https://doi.org/10.1130/0016-7606(1990)102%3C0786:AAOEMT%3E2.3.CO;2.

Watt, L. E., Bland, P. A., Prior, D. J., and Russell, S. S. 2006. Fabric Analysis of Allende Matrix Using EBSD. *Meteoritics & Planetary Science* 41: 989–1001. https://doi.org/10.1111/j.1945-5100.2006.tb00499.x.

Winter, J. D. 2013. *Principles of Igneous and Metamorphic Petrology*. Essex: New Intern Pearson. https://books.google.be/books?id=HBWpBwAAQBAJ.

Zhou, W., Apkarian, R., Wang, Z. L., and Joy, D. 2007. Fundamentals of Scanning Electron Microscopy (SEM). In *Scanning Microscopy for Nanotechnology: Techniques and Applications*, edited by W. Zhou, and Z. L. Wang, 1–40. New York: Springer. https://doi.org/10.1007/978-0-387-39620-0_1.

Zieg, M. J., and Marsh, B. D. 2002. Crystal Size Distributions and Scaling Laws in the Quantification of Igneous Textures. *Journal of Petrology* 43: 85–101. https://doi.org/10.1093/petrology/43.1.85.

SUPPORTING INFORMATION

Additional supporting information may be found in the online version of this article.

Appendix S1. EBSD grain aspect ratios.

Appendix S2. Nakhlite images used to form QTA data set.